Super skew scattering in two-dimensional Dirac material systems with a flat band

Cheng-Zhen Wang, Hong-Ya Xu, and Ying-Cheng Lai

Phys. Rev. B **103**, 195439 — Published 27 May 2021

DOI: 10.1103/PhysRevB.103.195439

Super skew scattering in two-dimensional Dirac material systems with a flat band

Cheng-Zhen Wang,[1] Hong-Ya Xu,[1,2] and Ying-Cheng Lai[1,3,*]
[1]*School of Electrical, Computer and Energy Engineering,*
Arizona State University, Tempe, Arizona 85287, USA
[2]*Institute of Computational Physics and Complex Systems,*
Lanzhou University, Lanzhou, Gansu 730000, China
[3]*Department of Physics, Arizona State University, Tempe, Arizona 85287, USA*
(Dated: March 31, 2021)

The phenomenon of super scattering was previously found to arise in massless pseudospin-1 two-dimensional Dirac material systems with a flat band. Here we report the phenomenon of *super skew scattering* of massive pseudospin-1 quasiparticles, which does not arise in the corresponding massless system. In particular, the scatterer is electrically generated with a certain geometric shape, and the mass is induced by gap opening between the Dirac cones. Even for a circular scatterer, the occurrence of resonant states inside it can induce a sizable anomalous Hall current, which is associated with the gap opening. The striking finding is that, a significant reduction in the scatter size and/or the potential height does nothing to weaken the skew scattering and, for certain resonant states, even tends to strengthen the scattering. This phenomenon of *super skew scattering* in Dirac materials with a flat band is in stark contrast to the scattering of massive pseudospin-1/2 quasiparticles from the same configuration, where skew scattering is significantly weaker and a reduction in the scatterer strength can quickly diminish it. The phenomenon is established analytically for the case of a circular scatterer in the framework of continuum Hamiltonian, and is found to be robust for an elliptical scatterer, which is solved numerically by adopting the multiple-multipole method to massive pseudospin-1 scattering. Calculations of the electronic transport properties in the Lieb lattice system reveal the occurrence of a large anomalous Hall current as well, paving the way for experimental observation and test of super skew scattering. Because of the "skew" nature that is absent in massless pseudospin-1 systems, the phenomenon of super skew scattering in massive systems can be exploited for applications in novel electronic or photonic Hall devices.

I. INTRODUCTION

Two-dimensional (2D) Dirac materials with quasiparticles whose motions are described by the laws of relativistic quantum mechanics are at the frontier of condensed matter physics and materials science. Such materials range from graphene[1] to three-dimensional (3D) topological insulators[2,3] and 3D Dirac and Weyl semimetals[4,5], where the quasiparticles are pseudospin-1/2 Dirac fermions. Dirac materials hosting pseudospin-1 quasiparticles have also been studied[6–33]. So far, pseudospin-1 materials uncovered include specially engineered photonic crystals[12,15,16,18,21], optical dice or Lieb lattices with loaded ultracold atoms[6–8,10,34], and certain electronic materials[13,14,19,20]. Distinct from massless pseudospin-1/2 Dirac material systems that exhibit "conventional" relativistic quantum phenomena as stipulated by the standard Dirac equation for spin-1/2 particles, in pseudospin-1 systems unusual physical phenomena can arise such as super Klein tunneling associated with one-dimensional barrier transmission[7,9,21,35], diffraction-free wave propagation and novel conical diffraction[12,15,16,18], flat-band induced conductivity[36–38], unconventional Anderson localization[26,39,40], peculiar Landau-Zener Bloch oscillations induced by the flat band[41], and strange topological phases under external gauge fields or spin-orbit coupling[10,32,42–44].

Electronic transport and scattering in Dirac material systems have been extensively studied[45–55]. For example, a study of the scattering of massless pseudospin-1/2 Dirac electrons by a circular potential barrier revealed[53] that, for a scatterer of small radius, the scattering cross sections are dominated by quantum resonances but, for a large scatterer, the classical picture of reflection and refraction of rays applies, leading to phenomena such as caustics, rainbow, and critical scattering. In massless pseudospin-1 particle scattering from a circular potential barrier, phenomena such as revival resonances, perfect caustics as induced by super-Klein tunneling, and universal low-energy isotropic transport can arise[23], which do not occur in pseudospin-1/2 scattering systems.

In pseudospin-1/2 or pseudospin-1 materials, opening a gap can lead to intriguing phenomena such as the Anomalous Hall Effect (AHE), a fundamental transport behavior that occurs in solids with a broken time-reversal symmetry in a ferromagnetic phase due to spin-orbit coupling[56]. For example, QAHE (Quantum Anomalous Hall Effect) in graphene was predicted in the presence of Rashba spin-orbit coupling and an exchange field generated by Fe absorbed on top of graphene or by proximity coupling to an antiferromagnetic insulator[57,58], where the exchange splitting is about 70 meV. AHE in single-layer graphene exchange-coupled to an atomically flat yttrium iron garnet (YIG) ferromagnetic thin film or to a magnetic nanoparticle array was realized in experiments[59,60]. Light induced AHE in monolayer graphene driven by ultrafast pulses of circularly polarized light was discovered experimentally[61] and explained theoretically[62], whose physical origin lies in light induced topological nontrivial Floquet-Bloch bands. In addition, there were studies on the extrinsic spin Hall effect induced by resonant skew scattering through spin-orbit coupling in graphene decorated by adatoms[63]. For pseudospin-1 systems, there are multiple mechanisms to open a gap: added on-site energy[7], introducing dimerization term[44,64], intrinsic spin-orbit coupling[10,64], or staggered flux phases on the kagome lattice[65]. The unconventional topological phases related to the gap was also investigated[10,44,64], and anomalous chiral edge states and in-gap edge states were discovered in massive pseudospin-1 systems[30,31]. Bounded electronic states were found in a gapped pseudospin-1 system with a centrally symmetric potential well and a regularized Coulomb potential induced by the charged impurities[66]. The phenomenon of super-Klein tunneling can occur even for massive pseudospin-1 particles[67]. Unconventional quantum Hall effect was studied in gapped pseudospin-1 systems with an infinite degeneracy of zero-energy Landau levels lifted into a series of bands[68].

Notwithstanding the existing work, quantum transport and scattering in massive pseudospin-1 systems have not been systematically studied, especially with respect to skew scattering as related to AHE. The purpose of this paper is to fill this gap. In particular, we investigate massive pseudospin-1 wave scattering from a finite size electrostatic potential barrier (realized by a proper gate voltage in experiments) in the deep subwavelength regime where the scatterer size is smaller than the wavelength. We find the occurrence of resonant modes inside the potential domain, associated with which is a quite appreciable skew scattering (Hall) current. The peak Hall current value obeys a scaling law with the potential properties. To test the robustness of the Hall current, we numerically study an elliptic potential barrier and find that the resonance-induced scattering peaks persist. In fact, due to breaking of the rotational symmetry, two sets of peaks emerge. For comparison, we also study the scattering of massive pseudospin-1/2 particles but find a vanishingly small Hall current as the result of absence of any resonant states. To test the feasibility of experimental observation of this "super-skew-scattering" phenomenon uncovered using a continuum Hamiltonian for pseudospin-1 wave scattering, we employ a finite size Lieb lattice device with a barrier generated by a gate potential, where gap opening is induced through the mechanisms of dimerization or spin-orbit coupling. We find that the resonant states leading to a large Hall current peak persist, which is particularly pronounced in the dimerization case. These findings have potential applications in AHE based devices.

II. SCATTERING HAMILTONIAN AND ANALYTIC CROSS SECTIONS FOR A CIRCULAR POTENTIAL

The 2D scattering system of massive pseudospin-1 quasiparticle from a scalar potential barrier of a given geometric shape is schematically illustrated in Fig. 1. The barrier shape is defined by the potential function $V(\boldsymbol{r})$, where $\boldsymbol{r}$ represents the position in the plane. The continuum massive pseudospin-1 Hamiltonian with a single Dirac point can be written as

$$H = \hbar v_F \boldsymbol{S} \cdot \boldsymbol{k} + \Delta S_z + V(\boldsymbol{r}), \tag{1}$$

where v_F is the magnitude of the group velocity associated with the Dirac cone, $\boldsymbol{k} = (k_x, k_y)$ denotes the wave vector, and Δ is the size of the energy gap between the flat and upper (lower) bands. The vector of matrices, $\boldsymbol{S} = (S_x, S_y)$, along with the third matrix S_z, forms a complete representation of spin-1 quasiparticles with the angular momentum commutation relations: $[S_l, S_m] = i\epsilon_{lmn} S_n$. The free-space energy-momentum dispersion relations in the presence of the energy gap Δ and a constant scalar potential V are

$$E = V, \tag{2}$$

$$E = \pm\sqrt{\hbar^2 v_F^2 (k_x^2 + k_y^2) + \Delta^2} + V, \tag{3}$$

as illustrated in Fig. 1(a).

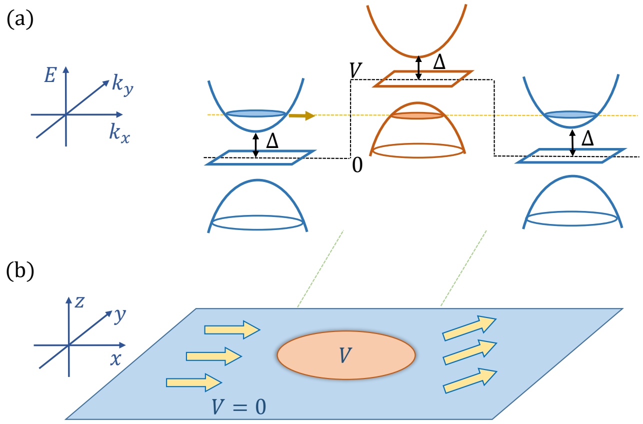

FIG. 1. Schematic illustration of massive pseudospin-1 particle scattering. (a) The energy-momentum dispersion relations in distinct spatial regions. (b) 2D scattering from a scatterer formed by a scalar gate potential.

The scattering process can be fully characterized by a number of cross sections: the differential, total, transport and skew cross sections, denoted as $d\sigma/d\theta$, σ, σ_{tr} and σ_{skew}, respectively. For the case of a circular, constant potential barrier, these cross sections of pseudospin-1 system can be calculated analytically. In particular, let V and R be the height and radius of the 2D potential barrier, respectively. The potential function is given by

$$V(\boldsymbol{r}) = V\Theta(R - r), \tag{4}$$

where Θ is the Heaviside function. The generalized Pauli matrices S_x, S_y, and S_z for spin-1 quasiparticles are

$$S_x = \frac{1}{\sqrt{2}} \begin{pmatrix} 0 & 1 & 0 \\ 1 & 0 & 1 \\ 0 & 1 & 0 \end{pmatrix}, \quad S_y = \frac{1}{\sqrt{2}} \begin{pmatrix} 0 & -i & 0 \\ i & 0 & -i \\ 0 & i & 0 \end{pmatrix}, \tag{5}$$

and

$$S_z = \begin{pmatrix} 1 & 0 & 0 \\ 0 & 0 & 0 \\ 0 & 0 & -1 \end{pmatrix}. \tag{6}$$

The Hamiltonian matrix in the polar coordinates is

$$H = -\frac{\hbar v_F}{\sqrt{2}} \tag{7}$$

$$\cdot \begin{pmatrix} \frac{-\sqrt{2}(\Delta+V)}{\hbar v_F} & e^{-i\theta}(i\partial_r + \frac{1}{r}\partial_\theta) & 0 \\ e^{i\theta}(i\partial_r - \frac{1}{r}\partial_\theta) & \frac{-\sqrt{2}V}{\hbar v_F} & e^{-i\theta}(i\partial_r + \frac{1}{r}\partial_\theta) \\ 0 & e^{i\theta}(i\partial_r - \frac{1}{r}\partial_\theta) & \frac{-\sqrt{2}(-\Delta+V)}{\hbar v_F} \end{pmatrix},$$

Because of the circular geometry of the electric potential scatterer, the total angular momentum

$$l = -i\hbar\partial_\theta + \hbar S_z (= 0, \pm 1, \pm 2, \ldots$$

is conserved. The partial wave component corresponding to l is

$$\psi_l(\boldsymbol{r}) = \begin{pmatrix} u_1 e^{i(l-1)\theta} \\ u_2 e^{ij\theta} \\ u_3 e^{i(l+1)\theta} \end{pmatrix}, \tag{8}$$

which enables a reduction of the Dirac equation $H\psi = E\psi$ to the following radial differential equation:

$$\frac{-\hbar v_F}{\sqrt{2}} \begin{pmatrix} \frac{-\sqrt{2}(\Delta+V-E)}{\hbar v_F} & i(\frac{\partial}{\partial r} + \frac{l}{r}) & 0 \\ i(\frac{\partial}{\partial r} - \frac{l-1}{r}) & \frac{-\sqrt{2}(V-E)}{\hbar v_F} & i(\frac{\partial}{\partial r} + \frac{l+1}{r}) \\ 0 & i(\frac{\partial}{\partial r} - \frac{l}{r}) & \frac{-\sqrt{2}(-\Delta+V-E)}{\hbar v_F} \end{pmatrix} \tag{9}$$

$$\cdot \begin{pmatrix} u_1 \\ u_2 \\ u_3 \end{pmatrix} = 0.$$

The corresponding eigenfunction is

$$\psi_l = C \begin{pmatrix} s_\tau F_{l-1}^\tau (k_\tau r) e^{-i\theta} \\ i\sqrt{2}\nu_\tau F_l^\tau (k_\tau r) \\ t_\tau F_{l+1}^\tau (k_\tau r) e^{i\theta} \end{pmatrix} e^{il\theta}, \tag{10}$$

where

$$k_\tau = \sqrt{(E - V_\tau)^2 - \Delta^2} / \hbar v_F, \tag{11}$$

$$s_\tau = -(\Delta - V_\tau + E)\hbar v_F k_\tau, \tag{12}$$

$$\nu_\tau = (\Delta + V_\tau - E)(\Delta - V_\tau + E), \tag{13}$$

$$t_\tau = -(\Delta + V_\tau - E)\hbar v_F k_\tau, \tag{14}$$

with $\tau = \text{I}$ or II denoting the exterior or interiors regions of the potential barrier, respectively. In the exterior region of the potential barrier, $F_l^I(k_I r) = H_l(k_I r)$ is the Hankel function of the first kind. In the potential region, $F_l^{II}(k_{II} r) = J_l(k_{II} r)$ is the Bessel function. Employing the method of partial wave decomposition, we can write the incident wave in the spinor spherical wave basis as

$$\Psi_{in} = \frac{N}{\sqrt{2}} \sum_l i^{l-1} \begin{pmatrix} s_I J_{l-1}(k_I r) e^{-i\theta} \\ i\sqrt{2}\nu_I J_l(k_I r) \\ t_I J_{l+1}(k_I r) e^{i\theta} \end{pmatrix} e^{il\theta}, \tag{15}$$

and the reflected wave as

$$\Psi_{ref} = \frac{N}{\sqrt{2}} \sum_l i^{l-1} A_l \begin{pmatrix} s_I H_{l-1}(k_I r) e^{-i\theta} \\ i\sqrt{2}\nu_I H_l(k_I r) \\ t_I H_{l+1}(k_I r) e^{i\theta} \end{pmatrix} e^{il\theta}, \tag{16}$$

with $J_l(x)$ and $H_l(x)$ being the Bessel and Hankel functions of the first kind, respectively. The transmitted wave inside the potential region is

$$\Psi_{tr} = \begin{pmatrix} \psi_1^{II} \\ \psi_2^{II} \\ \psi_3^{II} \end{pmatrix} \tag{17}$$

$$= \frac{N}{\sqrt{2}} \sum_l i^{l-1} B_l \begin{pmatrix} s_{II} J_{l-1}(k_{II} r) e^{-i\theta} \\ i\sqrt{2}\nu_{II} J_l(k_{II} r) \\ t_{II} J_{l+1}(k_{II} r) e^{i\theta} \end{pmatrix} e^{il\theta}.$$

The total wavefunction outside the scattering region ($r > R$) is given by

$$\Psi_I = \Psi_{in} + \Psi_{ref} = \begin{pmatrix} \psi_1^I \\ \psi_2^I \\ \psi_3^I \end{pmatrix} \tag{18}$$

$$= \frac{N}{\sqrt{2}} \sum_l i^{l-1} \begin{pmatrix} s_I [J_{l-1}(k_I r) + A_l H_{l-1}(k_I r)] e^{-i\theta} \\ i\sqrt{2}\nu_I [J_l(k_I r) + A_l H_l(k_I r)] \\ t_I [J_{l+1}(k_I r) + A_l H_{l+1}(k_I r)] e^{i\theta} \end{pmatrix} e^{il\theta}.$$

Utilizing the boundary conditions

$$\psi_2^I(R, \theta) = \psi_2^{II}(R, \theta), \tag{19}$$

$$\psi_1^I(R, \theta) + \psi_3^I(R, \theta) = \psi_1^{II}(R, \theta) + \psi_3^{II}(R, \theta), \tag{20}$$

we can obtain the coefficients A_l and B_l with the formula given in Appendix A.

In the far field, i.e., $r \gg R$, the spinor wave function can be written as

$$\Psi_I = N \begin{pmatrix} -\frac{s_I}{\sqrt{2}} \\ -\nu_I \\ \frac{t_I}{\sqrt{2}} \end{pmatrix} e^{ikr\cos\theta} + N \begin{pmatrix} -\frac{s_I}{\sqrt{2}} e^{-i\theta} \\ -\nu_I \\ \frac{t_I}{\sqrt{2}} e^{i\theta} \end{pmatrix} \frac{f(\theta)}{\sqrt{r}} e^{ikr}. \tag{21}$$

The reflected wave can be simplified as

$$\Psi_{ref} = N \sum_l -i^l A_l \sqrt{\frac{2}{\pi k_I r}} e^{i(k_I r - \frac{l\pi}{2} - \frac{\pi}{4})} \begin{pmatrix} -\frac{s_I}{\sqrt{2}} e^{-i\theta} \\ -\nu_I \\ \frac{t_I}{\sqrt{2}} e^{i\theta}, \end{pmatrix} e^{il\theta} \tag{22}$$

where we have used the approximate formula for the Hankel function of the first kind for $x \gg 1$:

$$H_\nu(x) \approx \sqrt{\frac{2}{\pi x}} e^{i(x - \frac{\nu\pi}{2} - \frac{\pi}{4})}. \tag{23}$$

This way, we obtain an explicit form for the function $f(\theta)$ as

$$f(\theta) = -\frac{e^{-i\pi/4}}{\sqrt{2\pi k}} \sum_{l=-\infty}^{\infty} 2A_l e^{il\theta}. \tag{24}$$

The differential, total, transport, and skew cross sections are given by

$$\frac{d\sigma}{d\theta} = |f(\theta)|^2 = \frac{2}{\pi k} |\sum_l A_l e^{il\theta}|^2, \tag{25}$$

$$\sigma = \int_0^{2\pi} |f(\theta)|^2 d\theta = \frac{4}{k} \sum_l |A_l|^2, \tag{26}$$

$$\begin{aligned} \sigma_{tr} &= \int_0^{2\pi} |f(\theta)|^2 (1 - \cos\theta) \\ &= \sigma - \frac{4}{k} \sum_l \Re[A_l A_{l+1}^*], \end{aligned} \tag{27}$$

$$\begin{aligned} \sigma_{skew} &= \int_0^{2\pi} d\theta |f(\theta)|^2 \sin\theta \\ &= \frac{4}{k} \sum_l \Im[A_l^* A_{l+1}], \end{aligned} \tag{28}$$

respectively, with $k = \sqrt{E^2 - \Delta^2}/\hbar v_F$.

III. EMERGENCE OF SUPER SKEW SCATTERING

A. Circular scatterer

1. *Far field behavior*

We first study a circular scatterer whose scalar potential barrier is defined by Eq. (4). As shown in Sec. II, due to the circular symmetry, the Dirac-Weyl equation can be analytically solved to yield the various scattering cross sections. For example, the skew scattering cross section is given by Eq. (28), which is determined by the coefficients A_l in the partial wave expansion. The formulas for these coefficients are quite sophisticated, posing an obstacle to understand the basic scattering physics.

To gain insights, we focus on the weak scattering regime where the size of the scatterer is smaller than the electron wavelength: $k_I R \ll 1$, $VR/\hbar v_F \ll 1$, and $k_{II} R \ll 1$. In this regime, the formulas for A_l and then for σ_{skew} can be simplified. Figure 2(a) shows σ_{skew} versus the incident electron energy for $VR = 0.256$ (with radius $R = 1$) and normalized mass $R\Delta = 0.064$. The choice of the value of VR can be arbitrary in a wide range to give qualitatively similar results. We set $R\Delta = VR/4$ for convenience. It can be seen that σ_{skew} exhibits three resonant peaks, one wide but relatively low and the two others narrow but high, for energy about $V_0/2$, indicating strong skew scattering near this energy value. The occurrence of skew scattering is indicative of the emergence of AHE for massive pseudospin-1 electrons scattered by an electric gate potential. In contrast, for pseudospin-1/2 scattering from the same configuration, no such resonant peaks in σ_{skew} arise and its overall values are much smaller than those for pseudospin-1 scattering in the entire energy interval, as shown in Fig. 2(b).

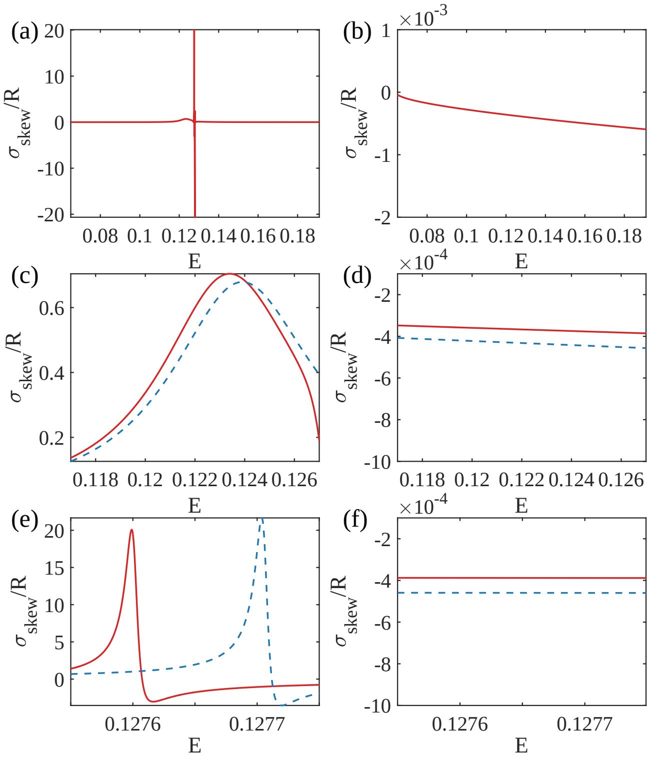

FIG. 2. Contrasting behaviors arising from the scattering of massive pseudospin-1 and that of pseudospin-1/2 quasiparticles from a circular gate potential scatterer in the Klein tunneling regime where the particle energy is about half of the potential height. The mass of the quasiparticles is $\Delta = 0.064$ and the gate potential is $V = 0.256$. (a) Skew scattering cross section σ_{skew} for massive pseudospin-1 quasiparticles versus incident energy, where resonant peaks arise. (b) The corresponding plot for pseudospin-1/2 scattering, where no resonant peaks occur and the values of σ_{skew} are much smaller than those in (a) in the entire energy range. (c) Magnification of the first resonant peak in (a), where the red solid and blue dashed curves are the numerical and analytic results, respectively. (d) The corresponding magnification for pseudospin-1/2 scattering with the same legends as in (c). (e) Magnification of the second resonant peak in (a). (f) The corresponding magnification for pseudospin-1/2 scattering.

Associated with the wider resonant peak in Fig. 2(a), the skew scattering is mainly contributed to by the interference between the $l = 0$ and $l = 1$ states. Focusing on the corresponding terms in Eq. (28), we get

$$\sigma_{skew} \approx \frac{4}{k}\Im[A_0 A_1^*] \approx \pi k R^2 \frac{V^2}{E^2}\frac{(V-E)(E-\Delta)+2\Delta E}{V(E+\Delta)}, \tag{29}$$

which is plotted as the dashed curve in Fig. 2(c), where the peak value is over 0.6. This analytic prediction agrees reasonably well with the numerical curve. The second (narrow and higher) peak in Fig. 2(a) is due to the interference between the $l = 1$ and $l = 2$ states. Focusing on this particular interference channel, we get

$$\sigma_{skew} \approx \frac{4}{k}\Im[A_1 A_2^*] \approx -\frac{4}{\pi}\frac{V-E+\Delta}{V}\frac{\ln\frac{\gamma k R}{2}}{k}, \tag{30}$$

with $\ln\gamma \approx 0.577$ being the Euler's constant, which is plotted as the blue dashed curve in Fig. 2(e). In comparison with the numerical curve (red solid), we observe a close resemblance between them, with a small difference in the peak position. In this case, the peak value of σ_{skew} is quite large, which is strong evidence for the emergence of super skew scattering. The details of the derivation and approximation of the analytic scattering formulas are given in Appendix A.

For scattering of massive pseudospin-1/2 quasiparticles, the analytic formula for the skew scattering cross section is (details in Appendix B)

$$\begin{aligned}\sigma_{skew} &= \frac{4}{k}\sum_{l}\Im[A_l A_{l+1}^*] \\ &\approx \frac{4}{k}\Im[A_0 A_1^*] = -\frac{\pi^2}{8}\frac{V^3\Delta}{k}(E^2-\Delta^2),\end{aligned} \tag{31}$$

which agrees well with the numerical result, as shown in Figs. 2(d) and 2(f) for the same energy intervals as in Figs. 2(c) and 2(e), respectively. In stark contrast to the scattering of pseudospin-1 quasiparticles, there are no resonant peaks and the value of σ_{skew} is about 4×10^{-4}, which is over three orders of magnitude smaller than those of the former.

2. *Near-field scattering behavior*

To reveal the near-field behavior, we calculate the probability and current distributions of the states corresponding to the first (wide) and second (narrow) resonant peaks in Fig. 2(a). The probability distribution can be written as $P = \Psi^\dagger\Psi$, where $\Psi = (\psi_1, \psi_2, \psi_3)^T$ is the wavefunction for points inside and outside the potential area, respectively, as given by Eqs. (17) and (18). The probability current operator is $\hat{\boldsymbol{J}} = \nabla_{\boldsymbol{p}} H = v_F(S_x, S_y)$, so the probability current density can be obtained as

$$\begin{aligned}\boldsymbol{J} &= (J_x, J_y) \\ &= v_F\sqrt{2}[Re(\psi_1^*\psi_2 + \psi_2^*\psi_3), Im(\psi_1^*\psi_2 + \psi_2^*\psi_3)].\end{aligned} \tag{32}$$

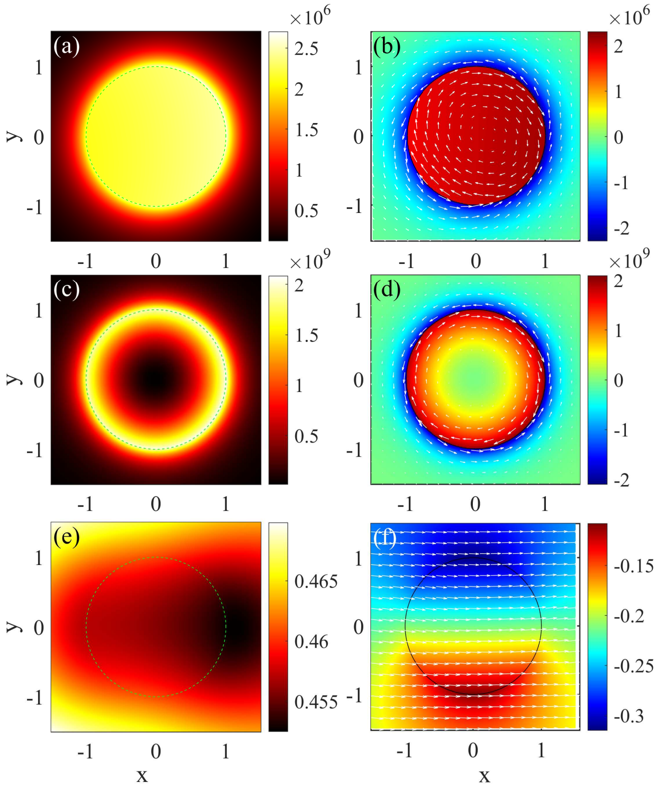

FIG. 3. Resonant state and current distribution for massive pseudospin-1 scattering from a circular potential barrier. (a) Probability density distribution of the first pseudospin-1 resonant state for $E = 0.1234$, and (b) the current density and spin-z density distributions, where the in-plane current is labeled by the white arrows and the out-of-plane pseudospin-z component is represented by the color map. (c) Probability density distribution for the second resonant state for $E = 0.1276$. (d) The corresponding current density and spin-z density distributions, with the same legends as in (b). (e) Probability density distribution of pseudospin-1/2 system for energy $E = 0.128$, and (f) the corresponding current and spin-z density distributions.

The probability density distribution of the spin-z component is given by

$$\langle\sigma_z\rangle = |\psi_1|^2 - |\psi_3|^2. \tag{33}$$

The results for the first peak are shown in Figs. 3(a) and 3(b) for the peak in Fig. 2(c) for energy $E = 0.1234$. It can be seen that the quasiparticles are mainly confined inside the potential area with a clockwise current, and the spin-z component is positive inside and negative outside. By further investigating the wavefunction form in Eqs. (17) and (18), we find that the main contribution to this probability distribution is the partial component of the angular momentum channel $l = 1$. As a result, the probability distribution is approximately circularly symmetric. The corresponding results for the second peak are shown in Figs. 3(c) and 3(d) for $E = 0.1276$. This resonance state is mostly confined about the edge area of the potential with a clockwise current inside and a counterclockwise current outside, and the spin-z component has different signs inside and outside the barrier. Moreover, the electron density is much larger than that associated with the first resonant state. We find that the main contribution to this state comes from the partial component of $l = 2$. In contrast, for pseudospin-1/2 quasiparticles, there is neither concentration of the probability density in the potential region nor that for the current, as shown in Figs. 3(e) and 3(f), indicating an absolute absence of any resonant scattering behavior. This lack of resonance is further confirmed by checking the partial component contributions, where a number of low angular momentum states contribute to this probability distribution. That is, pseudospin-1/2 quasiparticles effectively "see" no potential with near zero scattering.

3. Emergence of super skew scattering - scaling of skew cross section with scatterer strength

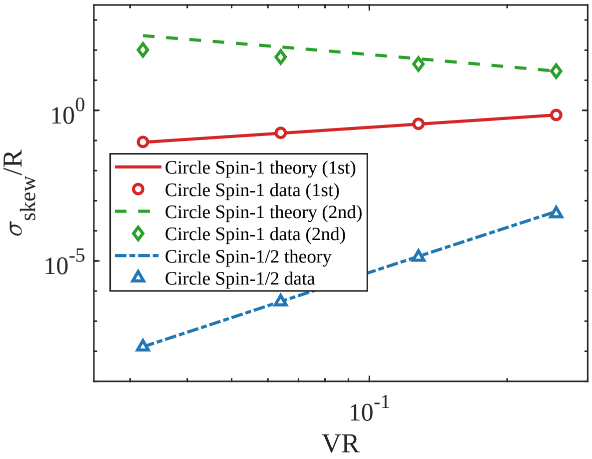

FIG. 4. Scaling of the resonant skew scattering cross section peak value with the strength of the circular scatterer. The red circles and green diamonds represent the numerical results for the first and second resonances of pseudospin-1 scattering, and the blue triangles are the corresponding results for pseudospin-1/2 scattering. The lines of the same colors are the theoretical predictions (not fittings). As the strength of the scatterer is weakened, the maximum value of the skew cross section decreases fast for pseudospin-1/2 scattering, but not so for pseudospin-1 scattering. In fact, for the second resonance peak in pseudospin-1 scattering (green), the skew scattering tends to intensify slightly as the scatterer becomes weaker. This scaling behavior signifies the emergence of super skew scattering of pseudospin-1 quasiparticles.

The analytical formulas for the skew scattering cross section for pseudospin-1 and pseudospin-1/2 quasiparticles [Eqs. (29-31)], together with the numerical support in Fig. 2, suggest certain scaling relationship between the cross section and the strength parameter VR of the scatterer. Figure 4 shows, on a log-log plot, the peak value of the effective skew scattering cross section σ_{skew}/R versus V_0R for three cases: pseudospin-1/2 scattering (blue) and resonant scattering associated with the first (red) and second (green) resonances in pseudospin-1 scattering [in Figs. 2(c) and 2(e), respectively]. Note that there are no peaks in the skew scattering cross section for pseudospin-1/2 particle, so we choose the energy to be $E = V/2$. In all three cases, there is a reasonably good agreement between the analytic predictions and the numerical results. For pseudospin-1/2 scattering (blue), the maximum value of σ_{skew}/R decreases rapidly as the strength of the scatterer is reduced: $\sigma_{skew}/R \sim (VR)^5$, which is characteristic of conventional quantum or light scattering. However, corresponding to the first resonance of pseudospin-1 scattering (red), the decrease in the value of the skew cross section is much slower with $\sigma_{skew}/R \sim VR$, indicating persistent super skew scattering when the scatterer is continuously weakened. The surprising phenomenon occurs for the second resonance of pseudospin-1 scattering (green), where skew scattering tends to intensify even as the scatterer strength is reduced, implying the presence of a large anomalous Hall current. A summary of the scaling of the peak value of skew and transport scattering cross section with the scatterer strength VR is given in Table I of Appendix C.

B. Elliptic scatterer

To test the robustness of resonant skew scattering for pseudospin-1 quasiparticles against geometric deformations, we consider an elliptical potential barrier. In this case, the scattering cross sections cannot be obtained analytically, and we use the multiple multipole method developed for treating the scattering of spin-1 and spin-1/2 particles from scatterers of an arbitrary geometric shape[30,55].

Far-field behavior. For comparison, we use the same values of the potential and mass as for the case of a circular scatterer: $V = 0.256$ and $\Delta = 0.064$, and set the area of the ellipse to be identical to that of the circle. Here, the ratio of the semi-minor axis b to the semi-major axis a is set to 0.6. The incident plane wave comes from the left to the right along the major axis of the ellipse. As shown in Fig. 5(a), for pseudospin-1 scattering, four resonant peaks arise in the pertinent energy interval: two wide and two narrow peaks, where one pair of wide-narrow peaks have their energy less than $V/2$ and the other pair larger than $V/2$. This should be compared with the case of a circular scatterer where the pair of resonant peaks have their energies approximately equal to $V/2$. The difference in the locations of the resonances notwithstanding, the occurrence of skew resonant scattering is robust against geometric deformations of the scatterer.

For pseudospin-1/2 scattering, no resonant peak exists in the skew scattering cross section, as shown in Fig. 5(b), which is similar to the case of a circular scatterer.

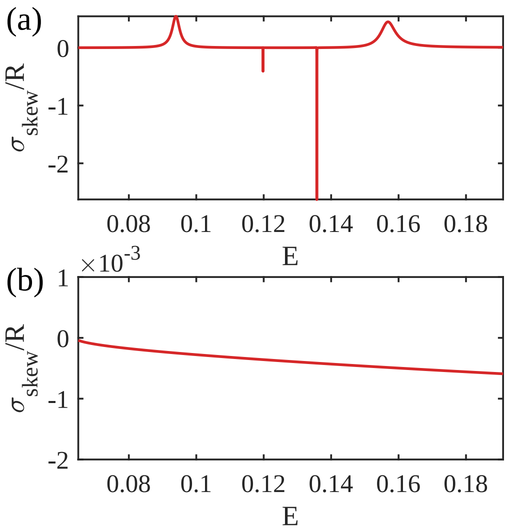

FIG. 5. Skew cross section versus energy E for scattering of massive Dirac quasiparticles from an elliptic gate potential barrier: (a) pseudospin-1 and (b) pseudospin-1/2. The uniform mass value is $\Delta = 0.064$ and the gate potential is $V = 0.256$ inside the elliptic barrier.

Near-field behavior. Figure 6 shows the distributions of the probability, current, and the out-of-plane component of the pseudospin for the four resonant states in Fig. 5(a) and for the corresponding pseudospin-1/2 scattering. The probability distribution for the first, wide resonant state is shown in Fig. 6(a), where the electron is uniformly distributed inside the potential region. Figure 6(b) shows that the current exhibits a vortex structure and is in the counterclockwise direction along the right and left edges of the barrier. It is this unidirectional current distribution that leads to the AHE. Figure 6(b) also shows that the z-component of the pseudospin is positive inside the barrier and negative outside. The probability distribution of the fourth wide resonant state is similar to that of the first state, as shown in Fig. 6(g), where the quasiparticles concentrate inside the barrier. The current is still counterclockwise, which forms vortices around the up and down parts of the barrier, as shown in Fig. 6(h). In addition, the z-component of pseudospin is negative inside the barrier region, in contrast to that associated with the first resonance. The corresponding results for the second and the third narrow resonance peaks are shown in Figs. 6(c-f), where the directions of the current for the two cases are the same. For the second peak, the current vortices occur at the four edges of the barrier (up, down, left, and right), while for the third peak, the vortices are in the up-left/right and down-left/right corners. The pseudospin-z directions are opposite for the two narrow resonance states. For pseudospin-1/2 scattering, no resonant states occur, nor do current vortices, as shown in Figs. 6(i) and 6(j), leading to near zero values of the skew scattering cross section.

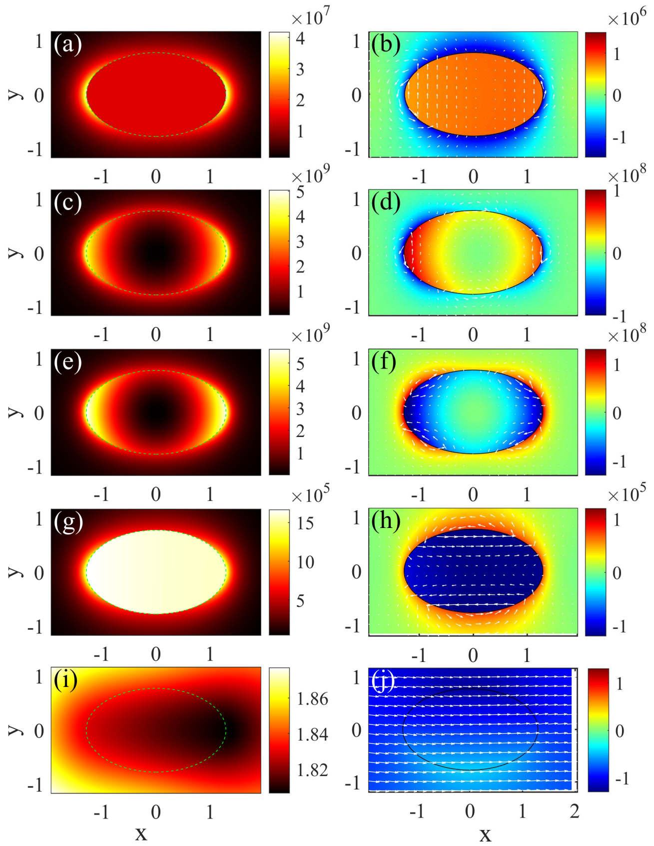

FIG. 6. Resonant state and current distribution for massive pseudospin-1 scattering from an elliptical potential barrier. (a,c,e,g) Probability density distribution for the pseudospin-1 resonant state for $E = 0.094$, 0.1198, 0.1357, and 0.1569, respectively. (b,d,f,h) The corresponding current density and spin-z density distributions, where the in-plane current is labeled with the arrows and the out-of-plane z component of the pseudospin is color represented. (i) Probability density distribution for pseudospin-1/2 scattering from an elliptical scatterer for $E = 0.128$ and (j) the corresponding current and pseudospin-z distributions.

Persistence of super skew scattering. Figure 7 shows the peak values of the four skew scattering resonances in Fig. 5(a) versus the scatterer strength. The data points from the four resonant states are nearly identical and, as the scatterer is weakened (by reducing the barrier height or its size, or both), the decrease in the peak cross section values roughly follow the scaling of $\sigma_{skew}/R \sim VR$, similar to the behavior of the first peak in the circular-potential case, which is indicative of super skew scattering that persists even when the circular potential barrier is deformed. In contrast, for pseudospin-1/2 quasiparticles, the maximum value of the skew cross section is small and decreases rapidly with the scatterer strength, as for the case of a circular barrier in Fig. 4. It is worth noting that skew scattering is robust against not only deformations of the scatterer shape, but also variations in the incident angles due to the resonant vortices formed about the potential area. (Further evidence is provided

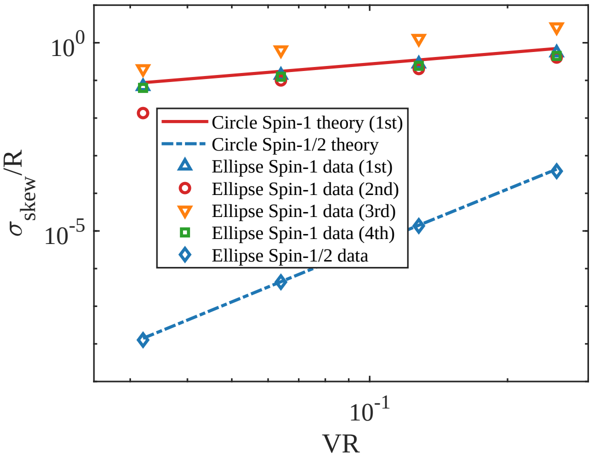

FIG. 7. Scaling of the peak value of skew scattering cross section with the strength of an elliptical electrical potential scatterer. The cross section is normalized by R, the radius of the circle with the same area as the ellipse, and the scatterer strength is VR ($R = 1$). The blue up-triangles, red circles, orange down-triangles, and green squares are the data points associated with the four skew scattering resonances in Fig. 5(a), respectively, from small to large energies. The red, green and blue lines are the theoretical results for circular scatterer, which serve as a reference. For pseudospin-1 quasiparticles, for all four resonant states, as the scatterer strength is reduced, the maximum value of the skew cross section decreases little, signifying super skew scattering. For pseudospin-1/2 quasiparticles (blue diamonds and dashed line), the maximum decreases rapidly and algebraically with the scatterer strength, which is typical of conventional quantum or light scattering.

in Appendix D.)

IV. SKEW RESONANT SCATTERING AND ANOMALOUS HALL EFFECT IN EXPERIMENTAL MASSIVE PSEUDOSPIN-1 LATTICE SYSTEMS

The results in Secs. II and III are from the effective, continuum Hamiltonian model for pseudospin-1 scattering where the system size is infinite. In experiments, pseudospin-1 systems are typically realized through lattices, e.g., photonic, electronic, or cold-atom lattices of finite size. To anticipate the theoretical and numerical results in Secs. II and III to occur in real physical systems, a prerequisite is to study if resonant skew scattering can arise in a finite lattice system. To be concrete, herein we study massive pseudospin-1 transport in a paradigmatic flat-band system: the Lieb lattice, as shown in Fig. 8(a). The relation between the single Dirac cone Hamiltonian of a Lieb lattice and that of a dice lattice can be found in Appendix E.

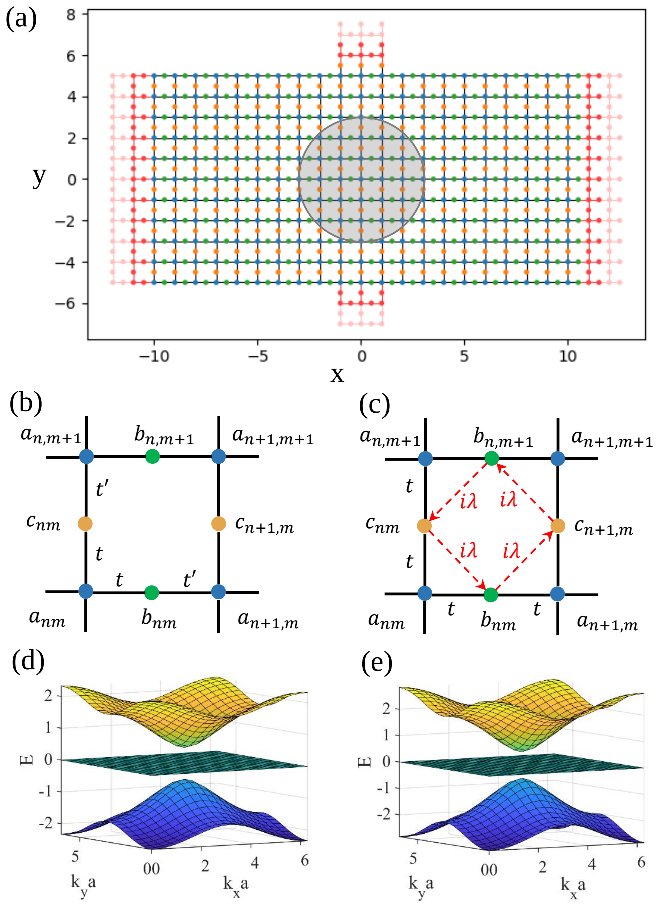

FIG. 8. Schematic illustration of an experimentally feasible, finite size lattice system for massive pseudospin-1 scattering. (a) General Lieb lattice structure. (b,c) Two mechanisms to generate massive pseudospin-1 quasiparticles: (b) dimerization and (c) imaginary next-nearest-neighbor interaction. (d,e) Band structures for the dimerized and imaginary next-nearest neighbor hopping Lieb lattices, respectively.

For an idealized Lieb lattice, the energy bands consist of a pair of vertex-touching Dirac cones and a flat band through the touching point, so the quasiparticles are of the massless pseudospin-1 type. When a gap opens between the two Dirac cones, the quasiparticles become massive. There are two methods to open up such a gap. The first one is through dimerization, which staggers different hopping amplitudes along the *a*-*b* and *a*-*c* directions, as shown in Fig. 8(b). The difference in the coupling strength breaks the C_4 symmetry of the lattice, leading to a gap opening. This is the 2D Su-Schrieffer-Heeger (SSH) model[44,64] with the following tight-binding Hamiltonian:

$$\begin{aligned} H = \sum_{n,m} & t a^{+}_{n,m} b_{n,m} + t' a^{+}_{n,m} b_{n-1,m} \\ & + t a^{+}_{n,m} c_{n,m} + t' a^{+}_{n,m} c_{n,m-1} + h.c. \end{aligned} \qquad (34)$$

where t and t' are the nearest neighbor coupling energies, $\{a^{+}_{n,m}, b^{+}_{n,m}, c^{+}_{n,m}\}$ and $\{a_{n,m}, b_{n,m}, c_{n,m}\}$ are the creation and annihilation operators for the localized states $|a_{n,m}\rangle$, $|b_{n,m}\rangle$, $|c_{n,m}\rangle$ of each atom, with n, m being the cell indices. In the momentum representation, the Hamiltonian is described by the following 3×3 matrix:

$$H = \tag{35}$$

$$\begin{pmatrix} 0 & te^{i\frac{k_x a}{2}} + t'e^{-i\frac{k_x a}{2}} & te^{i\frac{k_y a}{2}} + t'e^{-i\frac{k_y a}{2}} \\ te^{-i\frac{k_x a}{2}} + t'e^{i\frac{k_x a}{2}} & 0 & 0 \\ te^{-i\frac{k_y a}{2}} + t'e^{i\frac{k_y a}{2}} & 0 & 0 \end{pmatrix}.$$

The corresponding energy-momentum dispersion relation is

$$E_{\pm}(\boldsymbol{k}) = \pm\sqrt{4tt'\cos^2\frac{k_x a}{2} + 4tt'\cos^2\frac{k_y a}{2} + 2(t-t')^2}, \tag{36}$$

$$E_0(\boldsymbol{k}) = 0, \tag{37}$$

where $E_{\pm}$ are the energies of the upper and lower bands, respectively, E_0 is the flat band energy of the Lieb lattice, and a is lattice constant. Near the Dirac point $\boldsymbol{k} = (\frac{\pi}{a}, \frac{\pi}{a})$, the gap is the smallest with $\Delta = \sqrt{2}|t-t'|$. In the vicinity of the gap, the quasiparticles are described by the generalized, spin-1 Dirac-Weyl equation. The band structure is illustrated in Fig. 8(d).

The second method to open up a gap for the Lieb lattice is to introduce a purely imaginary next-nearest neighbor (NNN) hopping term[10,64] between atoms b and c with coupling strength λ , as shown in Fig. 8(c). Such interactions can be created via a magnetic flux[65] or spin-orbit coupling with only one spin component[10,69]. The tight-binding Hamiltonian is

$$\begin{aligned} H = \sum_{n,m} & ta^{+}_{n,m}b_{n,m} + ta^{+}_{n,m}b_{n-1,m} + ta^{+}_{n,m}c_{n,m} \\ & + ta^{+}_{n,m}c_{n,m-1} - i\lambda c^{+}_{n,m}b_{n,m} - i\lambda b^{+}_{n-1,m}c_{n,m} \\ & - i\lambda c^{+}_{n,m-1}b_{n-1,m} - i\lambda b^{+}_{n,m}c_{n,m-1} + h.c., \end{aligned} \tag{38}$$

and the momentum space Hamiltonian is

$$H = \tag{39}$$

$$\begin{pmatrix} 0 & 2t\cos\frac{k_x a}{2} & 2t\cos\frac{k_y a}{2} \\ 2t\cos\frac{k_x a}{2} & 0 & -i4\lambda\sin\frac{k_x a}{2}\sin\frac{k_y a}{2} \\ 2t\cos\frac{k_y a}{2} & i4\lambda\sin\frac{k_x a}{2}\sin\frac{k_y a}{2} & 0 \end{pmatrix},$$

with the energy-momentum dispersion relation given by

$$E_{\pm}(\boldsymbol{k}) = \tag{40}$$

$$\pm\sqrt{4t^2[\cos^2\frac{k_x a}{2} + \cos^2\frac{k_y a}{2}] + 16\lambda^2\sin^2\frac{k_x a}{2}\sin^2\frac{k_y a}{2}},$$

$$E_0(\boldsymbol{k}) = 0. \tag{41}$$

At the Dirac point, the gap size is $\Delta = 4\lambda$ and the corresponding band structure is schematically shown in Fig. 8(e).

We employ the Kwant package[70] to calculate the transport properties of massive pseudospin-1 particles on a finite Lieb lattice. We set the device length (in the horizontal direction) to be 80 lattice units and width (in the vertical direction) to be 40 units. The left and right leads have the same width as the device. To measure the Hall current, we set up two leads (up and down) with the width of two units. A circular gate potential is applied to the top of the device, whose radius is 10 units, with the potential height $V = 0.01$. The gap size is $\Delta = 0.0025$. The incident electron energy (normalized by the hopping energy t) varies from 0.0026 to 0.0099. The electrons come from the left lead, scatter from the device defined by the potential step, and leave the device through the right lead.

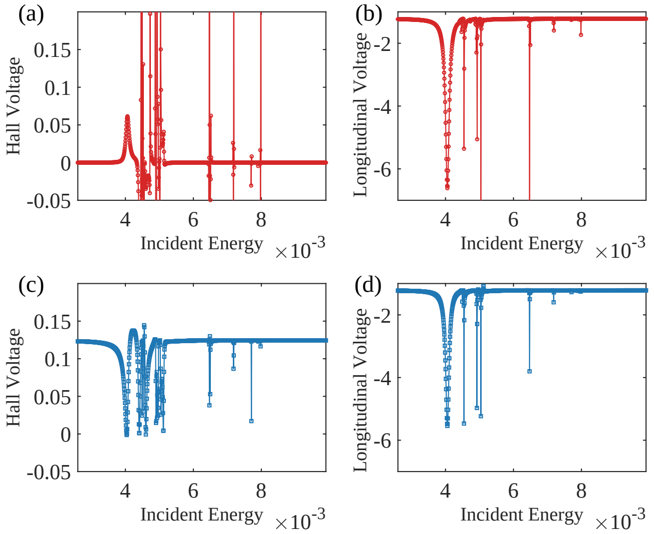

FIG. 9. Hall and longitudinal voltages of massive pseudospin-1 particles through a finite Lieb lattice device defined by an externally applied electrical potential. (a,b) Hall and longitudinal voltages versus the incoming electron energy for the dimerization gap-opening mechanism, respectively. (c,d) The corresponding results for the imaginary NNN hopping gap-opening mechanism.

Figures 9(a) and 9(b) show, for the dimer structure Lieb lattice, the Hall and longitudinal voltages versus the incident electron energy. The Hall voltage exhibits a large number of wide and narrow peaks, indicating the occurrence of Hall current (the Hall effect is anomalous because of the absence of any external magnetic field). The corresponding results for the imaginary NNN hopping Lieb lattice are shown in Figs. 9(c) and 9(d), where there are valleys below the constant Hall voltage, resulting from breaking of the time-reversal symmetry and the finite size effect.

We calculate the probability density and current distribution associated with the peak resonant state for incidence energy of $E = 0.0406$ (dimerization lattice) and $E = 0.0404$ (imaginary NNN hopping lattice). For the dimerized lattice scattering system, there is a concentration of pseudospin-1 electrons about the edge of the potential region, as shown in Fig. 10(a). Associated with the resonant state, there are current vortices around the top and bottom edges of the potential, as shown in

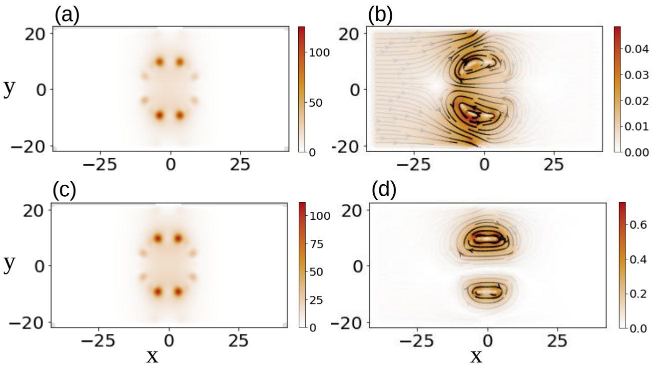

FIG. 10. Density and current distribution associated with resonant states. (a,b) Dimerization Lieb lattice with incident electron energy $E = 0.00406$. (c,d) Imaginary NNN hopping Lieb lattice with incident energy $E = 0.00404$.

Fig. 10(b), where the currents in the top and bottom vortices have opposite directions, signifying conservation of time-reversal symmetry. The corresponding results for the imaginary NNN hopping Lieb lattice are shown in Figs. 10(c) and 10(d). In this case, the currents associated with the top and bottom vortices have the same direction, as shown in Fig. 10(d), which is indicative of a broken time-reversal symmetry.

The results in Figs. 9 and 10 affirm that skew resonant scattering leading to anomalous Hall current can arise in experimentally realizable lattice systems hosting massive pseudospin-1 quasiparticles.

V. DISCUSSION

The phenomenon of superscattering in Dirac material systems has been theoretically predicted[25]. Specifically, in the subwavelength regime where the size of the scatterer is smaller than the wavelength, extraordinarily large values of the scattering cross section can arise even when the scatterer strength as measured by the product of its size with the potential height becomes arbitrarily small. This phenomenon occurs in two-dimensional Dirac material systems in which the quasiparticles are of the *massless* pseudospin-1 type, defying the conventional wisdom that wave scattering as characterized by the cross section should weaken continuously as the scatterer strength is reduced. The physical mechanism underlying superscattering was found[25] to be the emergence of a class of localized resonant modes inside the scatterer[23]. The energy band structure of the Dirac materials that host massless pseudospin-1 quasiparticles consists of a pair of Dirac cones with a flat band through the conical connecting point - the Dirac point, without gap opening. In experiments or real applications, various perturbations can be present which open a gap at the Dirac point, rendering *massive* the quasiparticles. The questions are whether the phenomenon of superscattering can persist and whether there are features that do not occur in the massless case.

Our study of massive pseudospin-1 scattering from an electrostatic potential barrier reveals the phenomenon of super skew scattering. Our method consists of two steps. First, for theoretical interest, we consider an effective continuum Hamiltonian system, in which an externally applied electrical field generates a potential barrier of either a circular or a deformed shape. In the former case, the wavefunctions and the relevant scattering cross sections can be solved analytically from the generalized spin-1 Dirac-Weyl equation through the approach of partial wave decomposition. Analytic and numerical results provide evidence for the occurrence of skew resonant scattering. The remarkable finding is the phenomenon of super skew scattering in which a decrease in the size and/or potential height of the scatterer does not lead to a reduction in the skew scattering cross section. When the circular scatterer is deformed so that the cross sections can be calculated only numerically, we find that the phenomenon of super skew scattering persists. We emphasize that skew scattering resonances and super scattering belong to the type of exotic physics unique to pseudospin-1 Dirac material systems with a flat band. In fact, we have demonstrated that such behaviors do not arise in pseudospin-1/2 systems (e.g., graphene).

Skew scattering is synonymous with AHE. In experiments, massive pseudospin-1 Dirac material systems are realized by finite size lattices and the Hall current is usually measured. We have thus studied a Lieb lattice system incorporating two distinct mechanisms to induce a band gap so that quasiparticles are of the pseudospin-1 type with a finite mass. We find that skew resonant scattering and anomalous Hall current can arise in the lattice systems, paving the way for experimentally observing and characterizing these phenomena. It should be noted the band topology can affect the transport behavior in a finite lattice system (Appendix F).

The phenomenon of resonant skew scattering in massive pseudospin-1 systems can be exploited for applications in Hall devices. For example, the skew scattering direction (or the direction of the anomalous Hall current) depends on the polarity of the applied electrical potential: by switching its polarity, the Hall current will be reversed. This may find applications in quantum sensing. Further, our work has revealed that, when the geometric shape of the scattering region is deformed from a perfect circle, a pair of wide resonant peaks with opposite z component of the pseudospin can arise for different incident energy. Tuning the incident energy can thus be used to control the direction of pseudospin.

We remark that, while adding mass to spin-1 fermions does not suppress the Klein tunneling effect, our work has revealed a key difference between the massless and massive cases: there is superscattering in the former but there is super skew scattering in the latter as induced by the gap opening. The main contribution of our work is an understanding of the skew scattering cross section resonances as a function of the incident energy through uncovering a scaling law characteristic of super skew scattering. The physical origin of the skew scattering resonances has also been elucidated in terms of certain angular momentum channels. Beyond the previously published massless, circular-scatterer case, the present work extends the study of massive spin-1 skew scattering to an elliptic shaped scatterer - a numerically challenging feat that we achieve by generalizing the multiple multipole method to massive spin-1 scattering. This is evidence that the phenomenon of super skew scattering is robust against geometric deformation of the scatterer. Another feature going beyond the previous work on massless spin-1 scattering is that, in the present work, electron transport in a finite Lieb lattice device has been studied to confirm that the phenomenon of super skew scattering can arise in experimentally feasible systems. Taken together, the results of this paper provide new insights into the relativistic quantum scattering of spin-1 particles with potential applications to anomalous Hall devices.

ACKNOWLEDGMENTS

This work was supported by the Pentagon Vannevar Bush Faculty Fellowship program sponsored by the Basic Research Office of the Assistant Secretary of Defense for Research and Engineering and funded by the Office of Naval Research through Grant No. N00014-16-1-2828.

Appendix A: Simplification of pseudospin-1 skew scattering formula

Using the partial wave decomposition method, we get the coefficient A_l and B_l for the scattering wave as

$$A_l = -\frac{\nu_I J_l(k_I R)[s_{II} J_{l-1}(k_{II} R) + t_{II} J_{l+1}(k_{II} R)] - \nu_{II} J_l(k_{II} R)[s_I J_{l-1}(k_I R) + t_I J_{l+1}(k_I R)]}{\nu_I H_l(k_I R)[s_{II} J_{l-1}(k_{II} R) + t_{II} J_{l+1}(k_{II} R)] - \nu_{II} J_l(k_{II} R)[s_I H_{l-1}(k_I R) + t_I H_{l+1}(k_I R)]}, \tag{A1}$$

$$B_l = \frac{\nu_I H_l(k_I R)[s_I J_{l-1}(k_I R) + t_I J_{l+1}(k_I R)] - \nu_I J_l(k_I R)[s_I H_{l-1}(k_I R) + t_I H_{l+1}(k_I R)]}{\nu_I H_l(k_I R)[s_{II} J_{l-1}(k_{II} R) + t_{II} J_{l+1}(k_{II} R)] - \nu_{II} J_l(k_{II} R)[s_I H_{l-1}(k_I R) + t_I H_{l+1}(k_I R)]}, \tag{A2}$$

where

$$s_\tau = \hbar v_F k_\tau (V_\tau - \Delta - E),\ t_\tau = -\hbar v_F k_\tau (V_\tau + \Delta - E),\ \nu_\tau = -(V_\tau + \Delta - E)(V_\tau - \Delta - E),\ k_\tau = \sqrt{\frac{(E - V_\tau)^2 - \Delta^2}{\hbar^2 v_F^2}}, \tag{A3}$$

with $\tau =$ I or II, corresponding to the region outside or inside the scatterer, respectively. For simplicity, we denote $x_1 = k_I R$ and $x_2 = k_{II} R$. The weak scattering regime can then be characterized by $x_1 \ll 1$ and $x_2 \ll 1$. For angular momentum $l = 0$, we have

$$\begin{aligned}
A_0 &= -\frac{\nu_I J_0(x_1)[s_{II} J_{-1}(x_2) + t_{II} J_1(x_2)] - \nu_{II} J_0(x_2)[s_I J_{-1}(x_1) + t_I J_1(x_1)]}{\nu_I H_0(x_1)[s_{II} J_{-1}(x_2) + t_{II} J_1(x_2)] - \nu_{II} J_0(x_2)[s_I H_{-1}(x_1) + t_I H_1(x_1)]} \\
&\approx -\frac{\nu_I[s_{II}(-\frac{x_2}{2}) + t_{II}\frac{x_2}{2}] - \nu_{II}[s_I(-\frac{x_1}{2}) + t_I\frac{x_1}{2}]}{\nu_I[1 + i\frac{2}{\pi}\ln\frac{\gamma x_1}{2}][s_{II}(-\frac{x_2}{2}) + t_{II}\frac{x_2}{2}] - \nu_{II}[s_I(-\frac{x_1}{2} + i\frac{2}{\pi}\frac{1}{x_1}) + t_I(\frac{x_1}{2} - i\frac{2}{\pi}\frac{1}{x_1})]} \\
&= -\frac{\frac{\nu_I}{2}x_2(t_{II} - s_{II}) - \frac{\nu_{II}}{2}x_1(t_I - s_I)}{\frac{\nu_I}{2}x_2(t_{II} - s_{II})[1 + i\frac{2}{\pi}\ln\frac{\gamma x_1}{2}] - \frac{\nu_{II}}{2}x_1(t_I - s_I)[1 - i\frac{4}{\pi}\frac{1}{x_1^2}]} \\
&\approx -\frac{\pi x_1^2}{\pi x_1^2 - i\frac{4E}{V} + i2\frac{V-E}{V}x_1^2\ln\frac{\gamma x_1}{2}},
\end{aligned} \tag{A4}$$

where Eq. (A3) have been used in Eq. (A4) to yield the final approximate results.

For angular momentum $l = 1$ with the corresponding coefficient A_1, we have

$$\begin{aligned}
A_1 &= -\frac{\nu_I J_1(x_1)[s_{II} J_0(x_2) + t_{II} J_2(x_2)] - \nu_{II} J_1(x_2)[s_I J_0(x_1) + t_I J_2(x_1)]}{\nu_I H_1(x_1)[s_{II} J_0(x_2) + t_{II} J_2(x_2)] - \nu_{II} J_1(x_2)[s_I H_0(x_1) + t_I H_2(x_1)]} \\
&\approx -\frac{\frac{\nu_I x_1}{2}[s_{II} + t_{II}\frac{x_2^2}{8}] - \frac{\nu_{II} x_2}{2}[s_I + t_I\frac{x_1^2}{8}]}{\nu_I[\frac{x_1}{2} - i\frac{2}{\pi}\frac{1}{x_1}][s_{II} + t_{II}\frac{x_2^2}{8}] - \frac{\nu_{II} x_2}{2}[s_I(1 + i\frac{2}{\pi}\ln\frac{\gamma x_1}{2}) + t_I(\frac{x_1^2}{8} - i\frac{4}{\pi}\frac{1}{x_1^2})]} \\
&\approx -\frac{\pi x_1^2}{\pi x_1^2 + i[4\frac{E-\Delta}{E+\Delta}\frac{V-2E}{V} + 2\frac{V+\Delta-E}{V}x_1^2\ln\frac{\gamma x_1}{2}]}.
\end{aligned} \tag{A5}$$

For A_{-1} with angular momentum $l = -1$, we have

$$\begin{aligned}
A_{-1} &= -\frac{\nu_I J_{-1}(x_1)[s_{II} J_{-2}(x_2) + t_{II} J_0(x_2)] - \nu_{II} J_{-1}(x_2)[s_I J_{-2}(x_1) + t_I J_0(x_1)]}{\nu_I H_{-1}(x_1)[s_{II} J_{-2}(x_2) + t_{II} J_0(x_2)] - \nu_{II} J_{-1}(x_2)[s_I H_{-2}(x_1) + t_I H_0(x_1)]} \\
&\approx -\frac{\frac{\nu_I x_1}{2}[t_{II} + s_{II}\frac{x_2^2}{8}] - \frac{\nu_{II} x_2}{2}[t_I + s_I\frac{x_1^2}{8}]}{\nu_I[\frac{x_1}{2} - i\frac{2}{\pi}\frac{1}{x_1}][t_{II} + s_{II}\frac{x_2^2}{8}] - \frac{\nu_{II} x_2}{2}[t_I(1 + i\frac{2}{\pi}\ln\frac{\gamma x_1}{2}) + s_I(\frac{x_1^2}{8} - i\frac{4}{\pi}\frac{1}{x_1^2})]} \\
&\approx -\frac{\pi x_1^2}{\pi x_1^2 + i[4\frac{E+\Delta}{E-\Delta}\frac{V-2E}{V} + 2\frac{(V-\Delta-E)}{V}x_1^2\ln\frac{\gamma x_1}{2}]}.
\end{aligned} \tag{A6}$$

For A_2 corresponding to the angular momentum $l = 2$, we have

$$\begin{aligned}
A_2 &= -\frac{\nu_I J_2(x_1)[s_{II} J_1(x_2) + t_{II} J_3(x_2)] - \nu_{II} J_2(x_2)[s_I J_1(x_1) + t_I J_3(x_1)]}{\nu_I H_2(x_1)[s_{II} J_1(x_2) + t_{II} J_3(x_2)] - \nu_{II} J_2(x_2)[s_I H_1(x_1) + t_I H_3(x_1)]} \\
&\approx -\frac{\frac{\nu_I x_1^2}{8}[s_{II}\frac{x_2}{2} + t_{II}\frac{x_2^3}{48}] - \frac{\nu_{II} x_2^2}{8}[s_I\frac{x_1}{2} + t_I\frac{x_1^3}{48}]}{\nu_I\frac{x_1^2}{8}[s_{II}\frac{x_2}{2} + t_{II}\frac{x_2^3}{48}] - \frac{\nu_{II} x_2^2}{8}[s_I\frac{x_1}{2} + t_I\frac{x_1^3}{48}] - i\frac{4}{\pi}\frac{\nu_I}{x_1^2}[s_{II}\frac{x_2}{2} + t_{II}\frac{x_2^3}{48}] + i\frac{\nu_{II} x_2^2}{8}[\frac{2}{\pi}\frac{s_I}{x_1} + \frac{16}{\pi}\frac{t_I}{x_1^3}]} \\
&\approx -\frac{\pi x_1^4}{\pi x_1^4 + i[32\frac{E-\Delta}{E+\Delta}\frac{V-2E}{V} - 4x_1^2\frac{V-E+\Delta}{V}(1 - \frac{1}{3}\frac{V-E+\Delta}{E+\Delta})]}.
\end{aligned} \tag{A7}$$

For A_{-2}, we have

$$A_{-2} = -\frac{\nu_I J_{-2}(x_1)[s_{II}J_{-3}(x_2) + t_{II}J_{-1}(x_2)] - \nu_{II}J_{-2}(x_2)[s_I J_{-3}(x_1) + t_I J_{-1}(x_1)]}{\nu_I H_{-2}(x_1)[s_{II}J_{-3}(x_2) + t_{II}J_{-1}(x_2)] - \nu_{II}J_{-2}(x_2)[s_I H_{-3}(x_1) + t_I H_{-1}(x_1)]}$$
$$\approx -\frac{\pi x_1^4}{\pi x_1^4 + i[32\frac{E+\Delta}{E-\Delta}\frac{V-2E}{V} - 4x_1^2\frac{V-E-\Delta}{V}(1-\frac{1}{3}\frac{V-E-\Delta}{E-\Delta})]}. \tag{A8}$$

The reflection amplitude can be obtained as

$$f(\theta) = -e^{-i\pi/4}\sqrt{\frac{2}{\pi k}}\sum_{l=-\infty}^{\infty} A_l e^{il\theta}. \tag{A9}$$

The differential cross section is given by

$$\frac{d\sigma}{d\theta} = |f(\theta)|^2 = \frac{2}{\pi k}|\sum_{l=-\infty}^{\infty} A_l e^{il\theta}|^2. \tag{A10}$$

The transport cross section is

$$\sigma_{tr} = \int_0^{2\pi} d\theta |f(\theta)|^2(1-\cos\theta)$$
$$= \frac{4}{k}\sum_l \left[|A_l|^2 - \Re(A_l A_{l+1}^*)\right]. \tag{A11}$$

The skew scattering cross section has the form

$$\sigma_{skew} = \int_0^{2\pi} d\theta |f(\theta)|^2 \sin\theta$$
$$= \frac{4}{k}\Im\left[\sum_l A_l^* A_{l-1}\right]. \tag{A12}$$

For the first resonant state in Fig. 2, the probability density distribution is confined inside the circular potential region. The transport cross section is dominated by the $l = 1$ term:

$$\sigma_{tr} \approx \frac{4}{k}|A_1|^2 \approx \frac{4}{k} = \frac{4}{\sqrt{E^2-\Delta^2}}, \tag{A13}$$

and skew scattering is the result of interference between the $l = 0$ and $l = 1$ states. We have

$$\sigma_{skew} \approx \frac{4}{k}\Im[A_0 A_1^*] \approx \pi k \frac{V^2}{E^2}\frac{(V-E)(E-\Delta) + 2\Delta E}{V(E+\Delta)}. \tag{A14}$$

For the second resonant state in Fig. 2, the $l = \pm 1$ and $l = 2$ states contribute to the transport cross section. We have

$$\sigma_{tr} = \frac{4}{k}\left[|A_{-1}|^2 + |A_1|^2 + |A_2|^2\right] \approx \frac{8}{k}. \tag{A15}$$

In this case, skew scattering is due to the interference between the $l = 1$ and $l = 2$ states. We have

$$\sigma_{skew} \approx \frac{4}{k}\Im[A_1 A_2^*] \approx -\frac{4}{\pi}\frac{V-E+\Delta}{V}\frac{\ln\frac{\gamma k}{2}}{k}. \tag{A16}$$

Appendix B: Massive pseudospin-1/2 scattering from a circular potential scatterer

For massive pseudospin-1/2 scattering[55], the reflection coefficient is

$$A_l = -\frac{\tau_1 J_l(x_1)J_{l-1}(x_2) - \tau_2 J_{l-1}(x_1)J_l(x_2)}{\tau_1 H_l(x_1)J_{l-1}(x_2) - \tau_2 H_{l-1}(x_1)J_l(x_2)}, \tag{B1}$$

where $l = j + \frac{1}{2}$, with $j = \pm\frac{1}{2}, \pm\frac{3}{2}, \ldots$, $x_1 = k_1 R$, $x_2 = k_2 R$, and

$$\tau_1 = -\frac{\hbar v_F k_1}{E-\Delta},\ \tau_2 = -\frac{\hbar v_F k_2}{E-V-\Delta},\ k_1 = \sqrt{\frac{E^2-\Delta^2}{\hbar^2 v_F^2}},\ k_2 = \sqrt{\frac{(E-V)^2-\Delta^2}{\hbar^2 v_F^2}},$$

with (x_1, τ_1, k_1) and (x_2, τ_2, k_2) being quantities corresponding to the area outside and inside the circular potential scatterer, respectively. In the weak scattering regime ($x_1 \ll 1$ and $x_2 \ll 1$), we have A_0 for $j = -1/2$ as

$$A_0 = -\frac{\tau_1 J_0(x_1)J_{-1}(x_2) - \tau_2 J_{-1}(x_1)J_0(x_2)}{\tau_1 H_0(x_1)J_{-1}(x_2) - \tau_2 H_{-1}(x_1)J_0(x_2)} \approx -\frac{-\pi\tau_1 x_1 x_2 + \pi\tau_2 x_1^2}{-\pi\tau_1 x_1 x_2 + \pi\tau_2 x_1^2 - i[4\tau_2 + 2\tau_1 x_2 x_1 \ln\frac{\gamma x_1}{2}]}$$
$$= -\frac{\pi V(E+\Delta)\sqrt{\frac{V-E-\Delta}{V-E+\Delta}}}{\pi V(E+\Delta)\sqrt{\frac{V-E-\Delta}{V-E+\Delta}} - i\left[4\sqrt{\frac{V-E-\Delta}{V-E+\Delta}} - 2\sqrt{\frac{E+\Delta}{E-\Delta}}\sqrt{(V-E)^2-\Delta^2}\,x_1\ln\frac{\gamma x_1}{2}\right]}. \tag{B2}$$

Similarly, for $j = 1/2$, we have

$$
\begin{aligned}
A_1 &= -\frac{\tau_1 J_1(x_1) J_0(x_2) - \tau_2 J_0(x_1) J_1(x_2)}{\tau_1 H_1(x_1) J_0(x_2) - \tau_2 H_0(x_1) J_1(x_2)} \approx -\frac{-\pi\tau_2 x_1 x_2 + \pi\tau_1 x_1^2}{-\pi\tau_2 x_1 x_2 + \pi\tau_1 x_1^2 - i[4\tau_1 + 2\tau_2 x_2 x_1 \ln\frac{\gamma x_1}{2}]} \\
&= -\frac{\pi V\sqrt{E^2-\Delta^2}}{\pi V\sqrt{E^2-\Delta^2} + i\big[-4\sqrt{\frac{E+\Delta}{E-\Delta}} + 2(V-E-\Delta)x_1 \ln\frac{\gamma x_1}{2}\big]}.
\end{aligned} \tag{B3}
$$

The relevant coefficient-dependent quantities can be approximated as

$$
\begin{aligned}
|A_0|^2 &\approx \frac{\pi^2 V^2}{16}(E+\Delta)^2, \\
|A_1|^2 &\approx \frac{\pi^2 V^2}{16}(E+\Delta)^2, \\
\Re[A_0 A_1^*] &\approx \frac{\pi^2 V^2}{16}(E^2-\Delta^2), \\
\Im[A_0 A_1^*] &\approx -\frac{\pi^3 V^3 \Delta}{32}(E^2-\Delta^2).
\end{aligned}
$$

The transport cross section is

$$
\begin{aligned}
\sigma_{tr} &= \frac{4}{k}\sum_l \left[|A_0|^2 + |A_1|^2 - \Re(A_l A_{l+1}^*)\right] \\
&\approx \frac{4}{k}\left[|A_0|^2 + |A_1|^2 - \Re(A_0 A_1^*)\right] \\
&= \frac{\pi^2}{4}\frac{V^2}{k}[E^2 + 3\Delta^2].
\end{aligned} \tag{B4}
$$

The skew scattering cross section has the form

$$
\begin{aligned}
\sigma_{skew} &= \frac{4}{k}\sum_l \Im[A_l A_{l+1}^*] \\
&\approx \frac{4}{k}\Im[A_0 A_1^*] = -\frac{\pi^2}{8}\frac{V^3\Delta}{k}(E^2-\Delta^2).
\end{aligned} \tag{B5}
$$

Appendix C: Transport cross sections

The results in the main text are for the skew cross sections. Here we present results for the transport cross sections in various cases. Figure 11 shows the behavior of the transport cross section for the same setting as in Fig. 2, and also shows the scaling of the peak transport cross section with the scatterer strength. It can be seen that there are super scattering associated with electron transport, similar to the massless case[25]. The scaling behavior of skew and transport cross sections with respect to circular scatterer strength is summarized in Table I. The results are based on Eqs. (A13), (A14), (A15), (A16), (B4) and (B5). Note that these formulas are valid in certain potential range. The scattering cross section should be zero when there is no potential. The corresponding results for the elliptic scatterer are shown in Figs. 12, where the phenomenon of super scattering persists.

TABLE I. Summary of the scaling of the peak value of skew and transport scattering cross sections with the scatterer strength VR.

	Spin-1 (1st)	Spin-1 (2nd)	Spin-1/2
σ_{skew}/R	VR	$\frac{\ln(\gamma VR)}{VR}$	$(VR)^5$
σ_{tr}/R	$(VR)^{-1}$	$(VR)^{-1}$	$(VR)^3$

Appendix D: Effect of varying incident angle for the case of an elliptical scatterer

For the elliptical scatterer, a different incident direction may affect the scattering cross sections. Surprisingly, we find that resonant skew scattering persists and changes little for different incident angles, as exemplified in Figs. 13(a) and 13(b), in spite of large variations in the transport cross section. The current distribution reveals that the vortices are similar for different incident angles, giving rise to robust vortices (or resonance) that lead to robust super skew scattering, as shown in Fig. 14.

Appendix E: Unitary transformation between the effective Hamiltonians of single Dirac-cone dice and Lieb lattices

In Secs. II and III, the effective Hamiltonian is derived from the a single Dirac cone dice lattice. In Sec. IV, the phenomenon of super skew scattering is observed in the single Dirac cone Lieb lattice. From a theoretical point of view, there exists a unitary transformation between the effective Hamiltonians of the single Dirac cone dice and Lieb lattices. Thus, in principle, results from the effective Hamiltonian of the single Dirac cone dice lattice are expected to hold when the effective Hamiltonian is one from the Lieb lattice. The results in Secs. II-IV thus demonstrate the generality of the phenomenon of super skew scattering across the two lattice systems. Here we present this unitary transformation.

For the dice lattice, the effective Hamiltonian is given by

$$
H^d = \hbar v_F \boldsymbol{S}^d \cdot \boldsymbol{k} + \Delta S_z + V(\boldsymbol{r}), \tag{E1}
$$

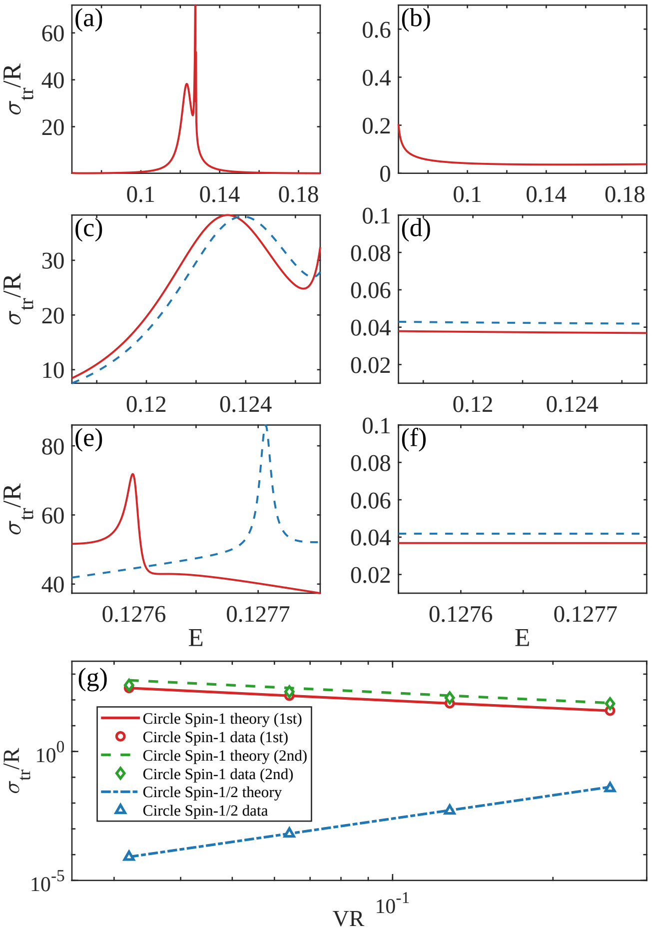

FIG. 11. Resonant transport cross section for massive pseudospin-1 scattering from a circular potential barrier in the Klein tunneling regime. The parameter values are the same as those in Fig. 2. (a) σ_{tr} for massive pseudospin-1 quasiparticles versus the incident energy. There are resonant peaks, corresponding to these in Fig. 2. (b) The corresponding plot for pseudospin-1/2 scattering, where no resonant peaks occur and the values of σ_{tr} are much smaller than those in (a) in the entire energy range. (c) Magnification of the first resonant peak in (a), where the red and blue dashed curves are the numerical and theoretical results, respectively. (d) The corresponding magnification for pseudospin-1/2 scattering with the same legends as in (c). (e) Magnification of the second resonant peak in (a). (f) The corresponding magnification for pseudospin-1/2 scattering. (g) Scaling of the resonant transport cross section peak value with the strength of the scatterer. The symbols are numerical data and the lines are the corresponding theoretical predictions.

with

$$S_x^d = \frac{1}{\sqrt{2}}\begin{pmatrix} 0 & 1 & 0 \\ 1 & 0 & 1 \\ 0 & 1 & 0 \end{pmatrix}, \quad S_y^d = \frac{1}{\sqrt{2}}\begin{pmatrix} 0 & -i & 0 \\ i & 0 & -i \\ 0 & i & 0 \end{pmatrix}, \tag{E2}$$

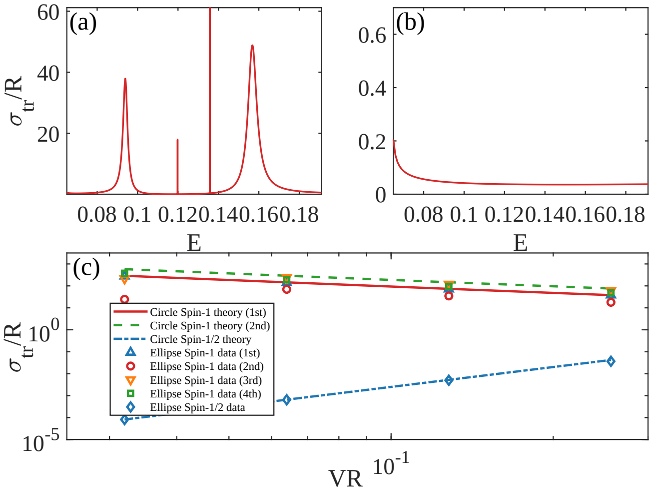

FIG. 12. Resonant transport cross section versus energy for scattering from an elliptical potential. (a) Pseudospin-1 system (b) Pseudospin-1/2 system. The parameter values are the same as those in Fig. 5. (c) Scaling of the resonant transport cross section peak value with the strength of the elliptical scatterer. Legends are the same as those in Fig. 7.

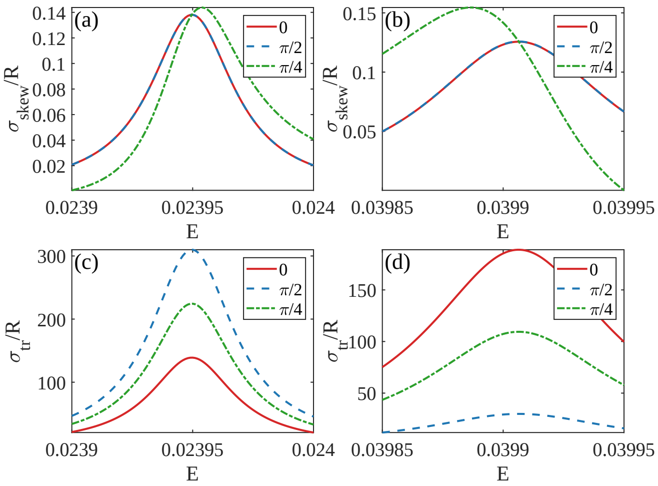

FIG. 13. Resonant skew and transport scattering cross sections for an elliptical scatterer for different incident angles. (a) Resonant skew scattering cross section for the first peak in Fig. 5. The red solid, blue dashed, and green dash-dotted curves are for the incident angles of 0 (along positive x direction), $\pi/2$ (along positive y direction), and $\pi/4$ (with respect to positive x direction), respectively. (b) The corresponding results for the fourth resonant peak in Fig. 5. (c) Resonant transport scattering cross section for the first peak in Fig. 12. The red solid, blue dashed, and green dash-dotted curves are for the incident angles of 0, $\pi/2$, and $\pi/4$, respectively. (d) The corresponding results for the fourth resonant peak in Fig. 12.

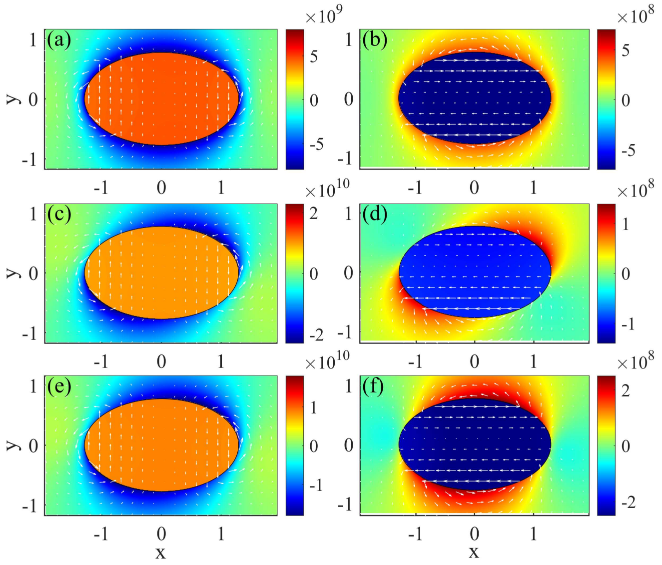

FIG. 14. In-plane current density and pseudospin-z distribution for different incident angles. (a,c,e) Results for the first resonant state in Fig. 5 for incident angle 0, $\pi/2$ and $\pi/4$. (b,d,f) Results for the fourth resonant state in Fig. 5 for the same set of incident angles.

and

$$S_z^d = \begin{pmatrix} 1 & 0 & 0 \\ 0 & 0 & 0 \\ 0 & 0 & -1 \end{pmatrix}. \tag{E3}$$

For the Lieb lattice, the effective Hamiltonian is

$$H^L = \hbar v_F \boldsymbol{S}^L \cdot \boldsymbol{k} + \Delta S_z + V(\boldsymbol{r}), \tag{E4}$$

with

$$S_x^L = \begin{pmatrix} 0 & 1 & 0 \\ 1 & 0 & 0 \\ 0 & 0 & 0 \end{pmatrix}, \quad S_y^L = \begin{pmatrix} 0 & 0 & 1 \\ 0 & 0 & 0 \\ 1 & 0 & 0 \end{pmatrix}, \tag{E5}$$

and

$$S_z^L = \begin{pmatrix} 0 & 0 & 0 \\ 0 & 0 & -i \\ 0 & i & 0 \end{pmatrix}. \tag{E6}$$

Consider the following unitary matrix:

$$U = \begin{pmatrix} 0 & 1 & 0 \\ \frac{1}{\sqrt{2}} & 0 & \frac{1}{\sqrt{2}} \\ \frac{i}{\sqrt{2}} & 0 & -\frac{i}{\sqrt{2}} \end{pmatrix}, \tag{E7}$$

which satifies $U^\dagger U = I$. The unitary transformation for the S-matrix can be expressed as

$$U^\dagger S_x^L U = S_x^d, \tag{E8}$$

$$U^\dagger S_y^L U = S_y^d, \tag{E9}$$

$$U^\dagger S_z^L U = S_z^d. \tag{E10}$$

The effective Hamiltonians from the two lattice systems can thus be connected by the unitary transformation

$$U^\dagger H^L U = H^d, \tag{E11}$$

with the current operator defined as

$$\hat{\boldsymbol{J}} = \nabla_{\boldsymbol{p}} H. \tag{E12}$$

The conclusion is that the far field scattering behavior and near field probability and current distributions are identical for the single Dirac-cone dice and Lieb lattices.

Appendix F: Topological effect on super skew scattering

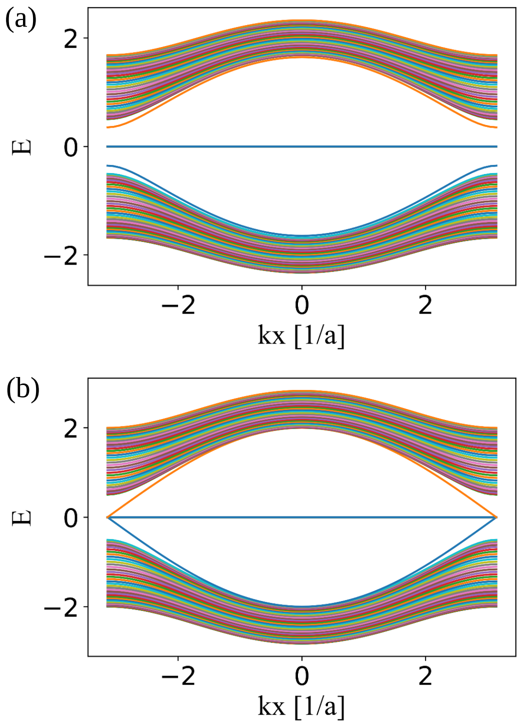

FIG. 15. Energy band structures of Lieb lattice under two gap-opening mechanisms. The lattice system is a strip that has the width of 40 lattice constants in the y direction and is infinite along the x direction. (a) Dimerization Lieb lattice and (b) Imaginary NNN hopping Lieb lattice. Here, for the illustrative purpose, the band gap size is chosen to be relatively large.

In Sec. IV, two gap-opening methods are employed for the Lieb lattice system: exploiting the dimerization term and adding a purely imaginary next-nearest neighbor hopping term. The topological properties of these two types of lattices are different. The dimerization lattice is topologically trivial while the lattice system with the imaginary NNN hopping is topologically nontrivial. A detailed discussion of the topological properties of these two cases can be found in Ref. [64]. For the finite device in our study, we calculate the energy band for a strip that is finite in the y direction and infinite along the x direction, as shown in Fig. 15. It can be seen that there is an empty gap for the dimerization lattice, while there is an edge mode for the imaginary NNN hopping lattice about $k_x = \pm\pi/a$. There is indication that the topology can have some effect on skew scattering for transport inside the energy band gap. In particular, as shown in Figs. 9(a) and 9(c), there is zero Hall voltage away from the resonance for the dimerization lattice, but there is a finite Hall voltage for the imaginary NNN hopping lattice when the energies are away from the resonance so it becomes a resonant valley. While the focus of this paper is on super skew scattering, the effect of topology deserves further attention.

---

[*] Ying-Cheng.Lai@asu.edu

[1] A. H. C. Neto, F. Guinea, N. M. R. Peres, K. S. Novoselov, and A. K. Geim, "The electronic properties of graphene," Rev. Mod. Phys. **81**, 109 (2009).

[2] M. Z. Hasan and C. L. Kane, "Colloquium: topological insulators," Rev. Mod. Phys. **82**, 3045 (2010).

[3] X.-L. Qi and S.-C. Zhang, "Topological insulators and superconductors," Rev. Mod. Phys. **83**, 1057 (2011).

[4] S.-Y. Xu, I. Belopolski, N. Alidoust, M. Neupane, G. Bian, C. Zhang, R. Sankar, G. Chang, Z. Yuan, C.-C. Lee, *et al.*, "Discovery of a Weyl fermion semimetal and topological Fermi arcs," Science **349**, 613 (2015).

[5] B. Lv, H. Weng, B. Fu, X. Wang, H. Miao, J. Ma, P. Richard, X. Huang, L. Zhao, G. Chen, *et al.*, "Experimental discovery of Weyl semimetal TaAs," Phys. Rev. X **5**, 031013 (2015).

[6] D. Bercioux, D. F. Urban, H. Grabert, and W. Häusler, "Massless dirac-weyl fermions in a $\mathcal{T}_3$ optical lattice," Phys. Rev. A **80**, 063603 (2009).

[7] R. Shen, L. Shao, B. Wang, and D. Xing, "Single Dirac cone with a flat band touching on line-centered-square optical lattices," Phys. Rev. B **81**, 041410 (2010).

[8] D. F. Urban, D. Bercioux, M. Wimmer, and W. Häusler, "Barrier transmission of Dirac-like pseudospin-one particles," Phys. Rev. B **84**, 115136 (2011).

[9] B. Dóra, J. Kailasvuori, and R. Moessner, "Lattice generalization of the Dirac equation to general spin and the role of the flat band," Phys. Rev. B **84**, 195422 (2011).

[10] N. Goldman, D. F. Urban, and D. Bercioux, "Topological phases for fermionic cold atoms on the Lieb lattice," Phys. Rev. A **83**, 063601 (2011).

[11] D. Bercioux, N. Goldman, and D. F. Urban, "Topology-induced phase transitions in quantum spin Hall lattices," Phys. Rev. A **83**, 023609 (2011).

[12] D. Guzmán-Silva, C. Mejía-Cortés, M. Bandres, M. Rechtsman, S. Weimann, S. Nolte, M. Segev, A. Szameit, and R. Vicencio, "Experimental observation of bulk and edge transport in photonic Lieb lattices," New J. Phys. **16**, 063061 (2014).

[13] W. Li, M. Guo, G. Zhang, and Y.-W. Zhang, "Gapless MoS_2 allotrope possessing both massless Dirac and heavy fermions," Phys. Rev. B **89**, 205402 (2014).

[14] G. Giovannetti, M. Capone, J. van den Brink, and C. Ortix, "Kekulé textures, pseudospin-one Dirac cones, and quadratic band crossings in a graphene-hexagonal indium chalcogenide bilayer," Phys. Rev. B **91**, 121417 (2015).

[15] R. A. Vicencio, C. Cantillano, L. Morales-Inostroza, B. Real, C. Mejía-Cortés, S. Weimann, A. Szameit, and M. I. Molina, "Observation of localized states in lieb photonic lattices," Phys. Rev. Lett. **114**, 245503 (2015).

[16] S. Mukherjee, A. Spracklen, D. Choudhury, N. Goldman, P. Öhberg, E. Andersson, and R. R. Thomson, "Observation of a localized flat-band state in a photonic Lieb lattice," Phys. Rev. Lett. **114**, 245504 (2015).

[17] S. Taie, H. Ozawa, T. Ichinose, T. Nishio, S. Nakajima, and Y. Takahashi, "Coherent driving and freezing of bosonic matter wave in an optical Lieb lattice," Sci. Adv. **1**, e1500854 (2015).

[18] F. Diebel, D. Leykam, S. Kroesen, C. Denz, and A. S. Desyatnikov, "Conical diffraction and composite Lieb bosons in photonic lattices," Phys. Rev. Lett. **116**, 183902 (2016).

[19] S. Paavilainen, M. Ropo, J. Nieminen, J. Akola, and E. Rasanen, "Coexisting honeycomb and kagome characteristics in the electronic band structure of molecular graphene," Nano Lett. **16**, 3519 (2016).

[20] L. Zhu, S.-S. Wang, S. Guan, Y. Liu, T. Zhang, G. Chen, and S. A. Yang, "Blue Phosphorene Oxide: Strain-tunable Quantum Phase Transitions and Novel 2D Emergent Fermions," Nano Lett. **16**, 6548 (2016).

[21] A. Fang, Z. Zhang, S. G. Louie, and C. T. Chan, "Klein tunneling and supercollimation of pseudospin-1 electromagnetic waves," Phys. Rev. B **93**, 035422 (2016).

[22] J. D. Malcolm and E. J. Nicol, "Frequency-dependent polarizability, plasmons, and screening in the two-dimensional pseudospin-1 dice lattice," Phys. Rev. B **93**, 165433 (2016).

[23] H.-Y. Xu and Y.-C. Lai, "Revival resonant scattering, perfect caustics, and isotropic transport of pseudospin-1 particles," Phys. Rev. B **94**, 165405 (2016).

[24] M. Tsuchiizu, "Three-dimensional higher-spin Dirac and Weyl dispersions in the strongly isotropic K_4 crystal," Phys. Rev. B **94**, 195426 (2016).

[25] H. Xu and Y.-C. Lai, "Superscattering of a pseudospin-1 wave in a photonic lattice," Phys. Rev. A **95**, 012119 (2017).

[26] A. Fang, Z. Q. Zhang, S. G. Louie, and C. T. Chan, "Anomalous Anderson localization behaviors in disordered pseudospin systems," Proc. Natl. Acad. Sci. **114**, 4087 (2017).

[27] C.-Z. Wang, H.-Y. Xu, L. Huang, and Y.-C. Lai, "Nonequilibrium transport in the pseudospin-1 Dirac-Weyl system," Phys. Rev. B **96**, 115440 (2017).

[28] D. Bercioux, O. Dutta, and E. Rico, "Solitons in one-dimensional lattices with a flat band," Ann. der Physik **529**, 1600262 (2017).

[29] C.-D. Han, H.-Y. Xu, D. Huang, and Y.-C. Lai, "Atomic collapse in pseudospin-1 systems," Phys. Rev. B **99**, 245413 (2019).

[30] H.-Y. Xu and Y.-C. Lai, "Pseudospin-1 wave scattering that defies chaos Q-spoiling and Klein tunneling," Phys.

Rev. B **99**, 235403 (2019).

[31] H.-Y. Xu and Y.-C. Lai, "Anomalous chiral edge states in spin-1 Dirac quantum dots," Phys. Rev. Research **2**, 013062 (2020).

[32] J. Hou, H. Hu, and C. Zhang, "Topological phases in pseudospin-1 fermi gases with two-dimensional spin-orbit coupling," Phys. Rev. A **101**, 053613 (2020).

[33] H.-Y. Xu and Y.-C. Lai, "Anomalous in-gap edge states in two-dimensional pseudospin-1 Dirac insulators," Phys. Rev. Research **2**, 023368 (2020).

[34] A. Raoux, M. Morigi, J.-N. Fuchs, F. Piéchon, and G. Montambaux, "From dia- to paramagnetic orbital susceptibility of massless fermions," Phys. Rev. Lett. **112**, 026402 (2014).

[35] C.-Z. Wang, C.-D. Han, H.-Y. Xu, and Y.-C. Lai, "Chaos-based Berry phase detector," Phys. Rev. B **99**, 144302 (2019).

[36] M. Vigh, L. Oroszlány, S. Vajna, P. San-Jose, G. Dávid, J. Cserti, and B. Dóra, "Diverging dc conductivity due to a flat band in a disordered system of pseudospin-1 Dirac-Weyl fermions," Phys. Rev. B **88**, 161413 (2013).

[37] W. Häusler, "Flat-band conductivity properties at long-range Coulomb interactions," Phys. Rev. B **91**, 041102 (2015).

[38] T. Louvet, P. Delplace, A. A. Fedorenko, and D. Carpentier, "On the origin of minimal conductivity at a band crossing," Phys. Rev. B **92**, 155116 (2015).

[39] J. Chalker, T. Pickles, and P. Shukla, "Anderson localization in tight-binding models with flat bands," Phys. Rev. B **82**, 104209 (2010).

[40] J. D. Bodyfelt, D. Leykam, C. Danieli, X. Yu, and S. Flach, "Flatbands under correlated perturbations," Phys. Rev. Lett. **113**, 236403 (2014).

[41] R. Khomeriki and S. Flach, "Landau-Zener Bloch oscillations with perturbed flat bands," Phys. Rev. Lett. **116**, 245301 (2016).

[42] F. Wang and Y. Ran, "Nearly flat band with Chern number $c = 2$ on the dice lattice," Phys. Rev. B **84**, 241103 (2011).

[43] H. Aoki, M. Ando, and H. Matsumura, "Hofstadter butterflies for flat bands," Phys. Rev. B **54**, R17296 (1996).

[44] C. Weeks and M. Franz, "Topological insulators on the Lieb and perovskite lattices," Phys. Rev. B **82**, 085310 (2010).

[45] M. Katsnelson, F. Guinea, and A. Geim, "Scattering of electrons in graphene by clusters of impurities," Phys. Rev. B **79**, 195426 (2009).

[46] J. Cserti, A. Pályi, and C. Péterfalvi, "Caustics due to a negative refractive index in circular graphene p- n junctions," Phys. Rev. Lett. **99**, 246801 (2007).

[47] M. Katsnelson and K. Novoselov, "Graphene: New bridge between condensed matter physics and quantum electrodynamics," Solid State Commun. **143**, 3 (2007).

[48] F. Guinea, "Models of electron transport in single layer graphene," J. Low Temp. Phys. **153**, 359 (2008).

[49] A. Matulis and F. Peeters, "Quasibound states of quantum dots in single and bilayer graphene," Phys. Rev. B **77**, 115423 (2008).

[50] P. Hewageegana and V. Apalkov, "Electron localization in graphene quantum dots," Phys. Rev. B **77**, 245426 (2008).

[51] J. H. Bardarson, M. Titov, and P. Brouwer, "Electrostatic confinement of electrons in an integrable graphene quantum dot," Phys. Rev. Lett. **102**, 226803 (2009).

[52] R. L. Heinisch, F. X. Bronold, and H. Fehske, "Mie scattering analog in graphene: Lensing, particle confinement, and depletion of Klein tunneling," Phys. Rev. B **87**, 155409 (2013).

[53] J.-S. Wu and M. M. Fogler, "Scattering of two-dimensional massless Dirac electrons by a circular potential barrier," Phys. Rev. B **90**, 235402 (2014).

[54] Y. Araki and K. Nomura, "Skyrmion-induced anomalous hall conductivity on topological insulator surfaces," Phys. Rev. B **96**, 165303 (2017).

[55] C.-Z. Wang, H.-Y. Xu, and Y.-C. Lai, "Scattering of Dirac electrons from a skyrmion: Emergence of robust skew scattering," Phys. Rev. Research **2**, 013247 (2020).

[56] N. Nagaosa, J. Sinova, S. Onoda, A. H. MacDonald, and N. P. Ong, "Anomalous Hall effect," Rev. Mod. Phys. **82**, 1539 (2010).

[57] Z. Qiao, S. A. Yang, W. Feng, W.-K. Tse, J. Ding, Y. Yao, J. Wang, and Q. Niu, "Quantum anomalous Hall effect in graphene from Rashba and exchange effects," Phys. Rev. B **82**, 161414 (2010).

[58] Z. Qiao, W. Ren, H. Chen, L. Bellaiche, Z. Zhang, A. H. MacDonald, and Q. Niu, "Quantum anomalous Hall effect in graphene proximity coupled to an antiferromagnetic insulator," Phys. Rev. Lett. **112**, 116404 (2014).

[59] Z. Wang, C. Tang, R. Sachs, Y. Barlas, and J. Shi, "Proximity-induced ferromagnetism in graphene revealed by the anomalous Hall effect," Phys. Rev. Lett. **114**, 016603 (2015).

[60] G. Song, M. Ranjbar, D. R. Daughton, and R. A. Kiehl, "Nanoparticle-Induced Anomalous Hall Effect in Graphene," Nano Lett. **19**, 7112 (2019).

[61] J. W. McIver, B. Schulte, F.-U. Stein, T. Matsuyama, G. Jotzu, G. Meier, and A. Cavalleri, "Light-induced anomalous Hall effect in graphene," Nat. phys. **16**, 38 (2020).

[62] S. Sato, J. McIver, M. Nuske, P. Tang, G. Jotzu, B. Schulte, H. Hübener, U. De Giovannini, L. Mathey, M. Sentef, *et al.*, "Microscopic theory for the light-induced anomalous Hall effect in graphene," Phys. Rev. B **99**, 214302 (2019).

[63] A. Ferreira, T. G. Rappoport, M. A. Cazalilla, and A. C. Neto, "Extrinsic spin Hall effect induced by resonant skew scattering in graphene," Phys. Rev. Lett. **112**, 066601 (2014).

[64] W. Beugeling, J. Everts, and C. M. Smith, "Topological phase transitions driven by next-nearest-neighbor hopping in two-dimensional lattices," Phys. Rev. B **86**, 195129 (2012).

[65] D. Green, L. Santos, and C. Chamon, "Isolated flat bands and spin-1 conical bands in two-dimensional lattices," Phys. Rev. B **82**, 075104 (2010).

[66] E. Gorbar, V. Gusynin, and D. Oriekhov, "Electron states for gapped pseudospin-1 fermions in the field of a charged impurity," Phys. Rev. B **99**, 155124 (2019).

[67] Y. Betancur-Ocampo, G. Cordourier-Maruri, V. Gupta, and R. de Coss, "Super-Klein tunneling of massive pseudospin-one particles," Phys. Rev. B **96**, 024304 (2017).

[68] Y. Xu and L.-M. Duan, "Unconventional quantum Hall effects in two-dimensional massive spin-1 fermion systems," Phys. Rev. B **96**, 155301 (2017).

[69] Y. He, J. Moore, and C. Varma, "Berry phase and anomalous Hall effect in a three-orbital tight-binding Hamiltonian," Phys. Rev. B **85**, 155106 (2012).

[70] C. W. Groth, M. Wimmer, A. R. Akhmerov, and X. Waintal, "Kwant: a software package for quantum transport," New J. Phys. **16**, 063065 (2014).